

Variational Quantum Metrology with Loschmidt Echo

Ran Liu,^{1,2} Ze Wu,^{1,2} Xiaodong Yang,^{3,4,5} Yuchen Li,^{1,2} Hui Zhou,⁶ Yuquan Chen,^{1,2} Haidong Yuan,^{7,*} Xinhua Peng,^{1,2,8,†} and Jiangfeng Du^{1,2,8}

¹CAS Key Laboratory of Microscale Magnetic Resonance and School of Physical Sciences, University of Science and Technology of China, Hefei 230026, China

²CAS Center for Excellence in Quantum Information and Quantum Physics, University of Science and Technology of China, Hefei 230026, China

³Shenzhen Institute for Quantum Science and Engineering, Southern University of Science and Technology, Shenzhen, 518055, China

⁴International Quantum Academy, Shenzhen, 518055, China

⁵Guangdong Provincial Key Laboratory of Quantum Science and Engineering, Southern University of Science and Technology, Shenzhen, 518055, China

⁶School of Physics, Hefei University of Technology, Hefei, Anhui 230009, China

⁷Department of Mechanical and Automation Engineering,

The Chinese University of Hong Kong, Shatin, Hong Kong SAR, China

⁸Hefei National Laboratory, University of Science and Technology of China, Hefei 230088, China

(Dated: November 23, 2022)

By utilizing quantum mechanical effects, such as superposition and entanglement, quantum metrology promises higher precision than the classical strategies. It is, however, practically challenging to realize the quantum advantages. This is mainly due to the difficulties in engineering non-classical probe state and performing nontrivial measurement in practise, particularly with a large number of particles. Here we propose a scalable scheme with a symmetrical variational quantum circuit which, same as the Loschmidt echo, consists of a forward and a backward evolution. We show that in this scheme the quantum Fisher information, which quantifies the precision limit, can be efficiently obtained from a measurement signal of the Loschmidt echo. We experimentally implement the scheme on an ensemble of 10-spin quantum processor and successfully achieves a precision near the theoretical limit which outperforms the standard quantum limit with 12.4 dB. The scheme can be efficiently implemented on various noisy intermediate-scale quantum devices which provides a promising routine to demonstrate quantum advantages.

To sense more accurately has always been one of the main drives for scientific advances and technological innovations. Quantum metrology [1–3], which utilizes quantum correlations to achieve quantum-enhanced sensitivities, has gained much attention recently. In ideal scenarios, quantum metrology can achieve a precision at the Heisenberg limit, which scales as $1/N$ with N as the number of particles [4–7], in contrast the precision of the classical strategies are bounded by the standard quantum limit (SQL), which scales as $1/\sqrt{N}$. To achieve such higher precisions, however, nontrivial entangled probe states need to be prepared. This poses a practically challenging task when the number of particles increases. The challenge is of two fold: first under general dynamics the complexity of identifying the optimal probe increases exponentially with the number of particle, thus the classical optimization that is used to search the optimal probe state soon becomes intractable due to the ‘curse of dimensionality’; second in practise due to device-specific constraints, such as the decoherence, imperfect control and readout errors, it is a challenging task to prepare the identified optimal probe state accurately, which leads to the deterioration of the performance [8–11].

Variational quantum metrology (VQM) provide a promising route to circumvent these problems. In VQM the identification of the optimal probe state is carried out with a hybrid quantum-classical scheme where the parameterized quantum circuit is used to prepare the probe state and only the parame-

ters are optimised externally by a classical optimization [12–18]. This hybrid scheme inherits the advantages of variational quantum algorithm which not only reduces the complexity of the classical simulation, but can also easily incorporate the device-specific constraints into the design of variational quantum circuit (VQC). The optimization of the parameters, however, is still very challenging for quantum metrology since the evaluation of the quantum Fisher information (QFI), which is typically taken as the figure of merit in quantum metrology, is a highly demanding task. The general brute-force approaches to extract QFI, such as quantum state tomography, demands an exponentially growing number of measurements [19]. Although this issue has been relieved somewhat with some effective surrogates of QFI previously, a considerable number of experimental measurements [20–23] or extra physical qubits [18, 24–26] are still required, which can go beyond the experimental capabilities.

In this Letter, we propose a scalable variational optimization scheme for quantum metrology which uses Loschmidt echo (LE) to efficiently extract the QFI. The signal of the LE can then be directly use to optimize the parameters of the VQC which prepares the optimal probe state in quantum metrology. We demonstrate the power of the scheme by identifying and preparing a 10-spin optimal probe state in NMR system, where the probe states are typically mixed under practical constraints, to estimate an unknown phase. We experimentally implement the scheme and demonstrate that the precision of this scheme

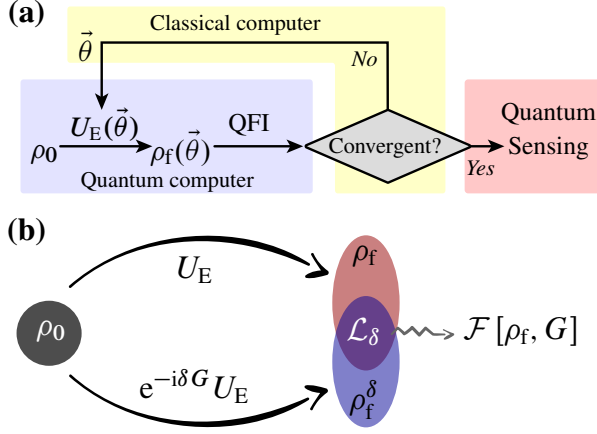


FIG. 1: (a). Workflow for quantum probe engineering via VQM. By taking the QFI as the figure of merit for the optimization of VQC, the probe state is steered to the optimal state for high precision phase estimation under practical dynamics. (b). Schematic diagram of measuring LE. When the unperturbed evolution is specified as the engineering operation, i.e., $U \rightarrow U_E(\vec{\theta})$, and the perturbation in the perturbed evolution is specified as a small quench under encoding dynamics, i.e., $U_\delta \rightarrow e^{-i\delta H} U_E(\vec{\theta})$, respectively, the QFI of the engineered probe ρ_f can then be extracted from LE .

saturates the fundamental bound in quantum metrology—the quantum Cramér-Rao bound (QCRB). This opens a promising avenue for the implementation of quantum enhanced parameter estimation on practical quantum devices due to its scalability, robustness against experimental imperfections and easy implementation.

Scheme.—We consider the iconic task of estimating the parameter α in the operator $U_\alpha = e^{-i\alpha H}$. The ultimate precision can be quantified by the QCRB, [1–3, 3, 27] as

$$\Delta\alpha \geq \frac{1}{\sqrt{\nu\mathcal{F}}}, \quad (1)$$

where $\Delta\hat{\alpha}$ is the standard deviation of an unbiased estimator $\hat{\alpha}$, ν is the number of repetitive measurements, \mathcal{F} is the QFI. Without loss of generality, we assume α is a small value since if it is not small we can always shift it with an additional field. Below we will also use δ to denote the value when we want to emphasize the value is small. Our target here is to engineering a probe state with the maximal QFI which leads to the smallest standard deviation. Here the probe state is prepared by a VQC which generates a unitary operation, $U_E(\vec{\theta})$, that acts on a natural initial state of the physical system, $\vec{\theta}$ are the parameters of the circuit that can be tuned. By taking the QFI as the figure of merit we then optimize these parameters of the variational circuit to steer the probe state towards the optimal or nearly optimal state which is subsequently used for high precision phase estimation. The schematic for the workflow of the quantum probe engineering via VQM is illustrated in Fig. 1(a). An essential part of the variational optimization is to efficiently evaluate the figure of merit that determines how the

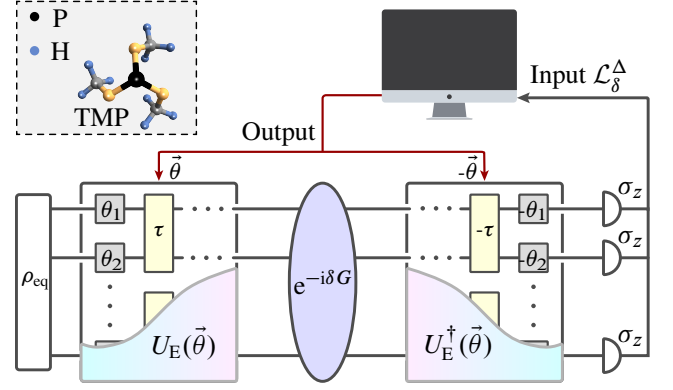


FIG. 2: The experimental procedures for variationally optimizing the metrologically useful mixed state via LE. The 10-spin quantum probe is realized by a ^{31}P nuclear spin and nine equivalent ^1H spins in TMP molecule and initialized as a equilibrium state ρ_{eq} . ρ_{eq} evolves under the symmetrical variational quantum circuit $V_\delta(\vec{\theta}) \equiv U_E^\dagger(\vec{\theta})e^{-i\delta H}U_E(\vec{\theta})$ and the polarization of each spin along z -axis then is measured to obtain the LE \mathcal{L}_δ . The QFI of quantum probe, i.e., $\mathcal{F}[\rho_f(\vec{\theta}), H]$, can be extracted from LE and feedback to the classical computer, which is employed to iteratively update the parameters $\vec{\theta}$ to maximize the QFI.

parameters should be tuned. However, the standard methods of evaluating the QFI, such as state tomography, are extremely demanding experimentally. Here we develop an experimental protocol that uses Loschmidt echo to evaluate the QFI. For pure state the Loschmidt echo is given by $\mathcal{L}_\delta = |\langle\Psi_0|U^\dagger U_\delta|\Psi_0\rangle|^2$, which is the overlap between the states obtained from the forward unperturbed evolution (U) and the forward perturbed evolution (U_δ). The Loschmidt echo corresponds to a susceptibility to a perturbation [28, 29]. As shown in Fig. 1(b), the Loschmidt echo can be used to quantify the QFI when the unperturbed evolution is replaced with the engineering operation, i.e., $U \rightarrow U_E(\vec{\theta})$, and the perturbation in the perturbed evolution is replaced with a small quench under encoding dynamics, i.e., $U_\delta \rightarrow e^{-i\delta H}U_E(\vec{\theta})$, respectively. In this case [30]

$$\mathcal{F}[U_E(\vec{\theta})|\Psi_0] = \lim_{\delta \rightarrow 0} 4 \frac{1 - \mathcal{L}_\delta}{\delta^2}. \quad (2)$$

For mixed states, the Loschmidt echo is given by

$$\begin{aligned} \mathcal{L}_\delta &\equiv \text{Tr}[\rho_f \rho_f^\delta] \\ &= \gamma(\rho_f) - \frac{\delta^2}{4} \times \left[2 \sum_{i,j=1}^d (\lambda_i - \lambda_j)^2 |\langle\psi_i|G|\psi_j\rangle|^2 \right] + o(\delta^4), \end{aligned} \quad (3)$$

where $\rho_f = U_E(\vec{\theta})\rho_0 U_E^\dagger(\vec{\theta}) = \sum_{i=1}^d \lambda_i |\psi\rangle\langle\psi|$, $\rho_f^\delta = e^{-i\delta H} U_E(\vec{\theta})\rho_0 U_E^\dagger(\vec{\theta}) e^{i\delta H}$, $\gamma(\rho_f) = \sum_{i=1}^d \lambda_i^2$ is the purity of state which, in our case, can be treated as a constant since it doesn't change under the unitary evolution, d is the dimension

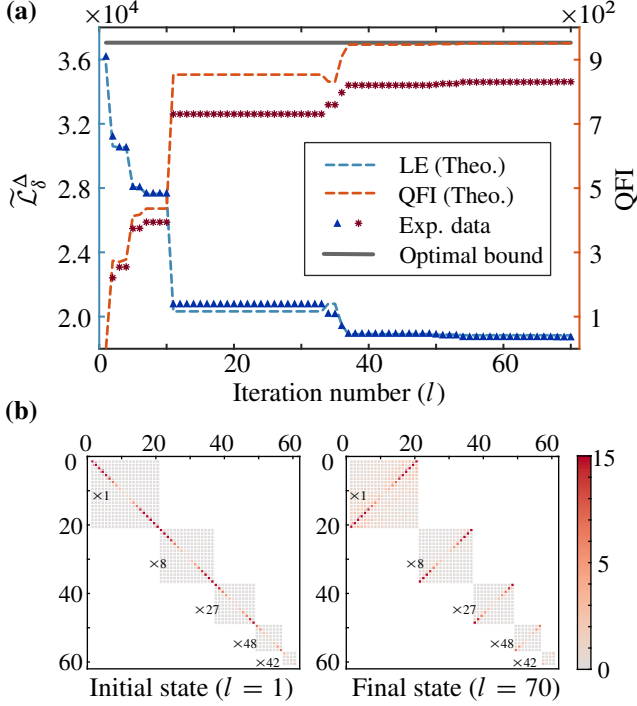


FIG. 3: (a). Experimental results of variational quantum optimization. The blue triangles are the measured $\mathcal{L}_\delta^\Delta$ in experiment. The loop is stopped until the number of iterations reaches 70. The blue dashed line is the theoretical LE obtained from numerical calculation to provide a benchmark for the experimental accuracy. The estimated QFI according to Eq. (5) is depicted with the red stars, while the red dashed line is the theoretical QFI. The optimal QFI [32] is plotted with the black solid line. The finally engineered probe is close to the optimal one even in the presence of experimental imperfections. (b) A brief representation of the derivation part of the initial state ρ_0^Δ and reconstructed engineered quantum state ρ_f^Δ . In contrast to ρ_0^Δ , ρ_f^Δ has more population on the anti-diagonal positions of density matrix, thus achieving a faster phase accumulation under $H = \sum_{k=1}^{10} \sigma_z^k / 2$.

of the Hilbert space. Compared to the QFI of the mixed-states, we have (see Supplementary Material for detailed derivation)

$$\mathcal{F}[\rho_f, H] \geq \lim_{\delta \rightarrow 0} 4 \frac{\gamma[\rho_f] - \mathcal{L}_\delta}{\delta^2}. \quad (4)$$

For pure states, this recovers Eq.(2) where the bound can be saturated. For highly mixed states where the eigenvalues are almost degenerate, i.e., $\lambda_i \approx \frac{1}{d}$ for $1 \leq i \leq d$, the bound can also be saturated with

$$\mathcal{F}[\rho_f, H] \approx \lim_{\delta \rightarrow 0} 2d \frac{\gamma[\rho_f] - \mathcal{L}_\delta}{\delta^2}. \quad (5)$$

This is exactly the case in NMR as the initial state of the NMR system is a thermal state with the Boltzmann distribution, which at the room-temperature is close to the completely mixed state [31]. Since $\rho_f = U_E(\vec{\theta})\rho_0 U_E^\dagger(\vec{\theta})$ has the same eigenvalue as ρ_0 , ρ_f is thus also almost degenerate.

We can rewrite the Loschmidt echo in Eq. (3) as

$$\mathcal{L}_\delta \equiv \text{Tr} \left[V_\delta(\vec{\theta})\rho_0 V_\delta^\dagger(\vec{\theta})\rho_0 \right] \quad (6)$$

with $V_\delta(\vec{\theta}) \equiv U_E^\dagger(\vec{\theta})e^{-i\delta H}U_E(\vec{\theta})$. The Loschmidt echo can thus be obtained by first using the variational quantum circuit to generate $U_E(\vec{\theta})$, then apply a perturbation evolution $e^{-i\delta H}$, followed by a backward $U_E(\vec{\theta})$ and a projection onto the initial state. We note that the initial state typically can be written as product states, the Loschmidt echo can thus be efficiently extracted with local measurements where the number of measurements increase linearly with the number of qubits.

Experimental variational optimization of 10-spin mixed-state quantum probe.— We experimentally demonstrate the scheme with nuclear spins at room temperature on a Bruker Avance III 400 MHz NMR spectrometer. The sample is trimethylphosphite (TMP) dissolved in d_6 acetone. The TMP molecule, which consists of a central ^{31}P nuclear spin and nine equivalent ^1H nuclear spins as shown in Fig. 2, is employed as the 10-spin quantum probe. The structure of the molecule is shown in Fig. 3. In the liquid state, the interaction between ^1H spins is negligible due to the magnetic equivalence. The natural Hamiltonian of the system in doubly rotating frame is $H_{\text{NMR}} = \frac{\pi}{2} J_{\text{PH}} \sigma_z^1 \otimes \sum_{j=2}^{10} \sigma_z^j$ with $J_{\text{PH}} = 10.5\text{Hz}$. Here the Pauli matrices for spin j are denoted by σ_ν^j ($\nu = x, y, z$), and a ^{31}P nuclear spin and nine ^1H nuclear spins are denoted by Arabic numerals 1 and 2,3,...10, respectively.

Fig. 2 shows the experimental procedures for engineering the mixed-state probe via the hybrid quantum-classical scheme with the quantum variational optimization. Here the evolutions and measurements are on the quantum system while the updating of the parameters are determined on the classical computer.

The system is initially at the equilibrium state of the room temperature, $\rho_{\text{eq}} = (\mathbb{1} + \epsilon \rho_{\text{eq}}^\Delta) / 2^{10}$ where $\rho_{\text{eq}}^\Delta = \sum_{j=1}^{10} \gamma_j \sigma_z^j$, $\mathbb{1}$ is the $2^{10} \times 2^{10}$ unit operator, ϵ is the thermal polarization ($\sim 10^{-5}$) and γ_j is the gyromagnetic ratio of the corresponding nuclear. We note that $\mathbb{1}$ in ρ_{eq} does not change under the unitary evolution, which is $V_\delta(\vec{\theta})$ in our case, it thus does not contribute to the experimental signal since the observables in NMR are traceless. With ρ_{eq} as the initial state, the Loschmidt echo in Eq. (6) then becomes

$$\mathcal{L}_\delta = \frac{1}{2^N} + \frac{\epsilon^2}{2^{2N}} \mathcal{L}_\delta^\Delta, \quad (7)$$

where $\mathcal{L}_\delta^\Delta \equiv \sum_{j=1}^{10} \gamma_j \text{Tr} \left(V_\delta(\vec{\theta})\rho_{\text{eq}}^\Delta V_\delta^\dagger(\vec{\theta})\sigma_z^j \right)$ can be experimentally obtained by measuring the polarization of the evolved system.

In our experiment, $U_E(\vec{\theta})$ is realized by a 3-layer VQC consisting of single-spin rotations, $e^{-i\theta_k \sigma_{x,y}/2}$ with $\vec{\theta} \equiv (\theta_1, \theta_2, \dots, \theta_k, \dots)$, and the free evolution under the Hamiltonian, H_{NMR} , that evolves with a duration τ . The details of this parameterized quantum circuit can be found in the Supplementary Material where we also analyzed the set of the states

that can be generated by this circuit and showed that it contains the optimal probe state. After the preparation of the optimal probe state, the dynamics that encodes the parameter, $e^{-i\delta H}$, is then applied. In the experiment the Hamiltonian is given by $H = \sum_{k=1}^{10} \sigma_z^k / 2$. Theoretically, the correspondence between the Loschmidt echo and the QFI is best when $\delta \rightarrow 0$, as shown in Eq. (5). However, the experiment signal of the Loschmidt echo is least sensitive to the change of the parameter when $\delta = 0$ since $\mathcal{L}_\delta = \gamma(\rho_f)$ reaches the maximal where the derivative is zero. So there exists a trade-off. With the aid of numerical simulation (see Supplementary Material for detail), we find that $\delta = 0.2$ is optimal for our experiment. After $e^{-i\delta H}$, a reverse evolution, $U_E(\vec{\theta})$, is then applied which is followed by the measurement, i.e., the projection to the initial state. The reverse evolution is realized by flipping the order of the parameterized circuit, which is experimentally achieved by reversing the phase of single-spin rotations and inserting π pulses for the free evolution [33]. The projection is achieved by measuring the polarization of each nuclear spin along z -axis. Since the nine ^1H spins are identical, their polarization can be obtained with a single measurement. From which $\mathcal{L}_\delta^\Delta$ can then be obtained which further gives the QFI of $\rho_f(\vec{\theta})$.

In our experiment, the single-spin rotations are realized with composited sequence of BB1 [33] which can reduce the errors caused by the imperfections of the pulse shapes. The protons are decoupled [34] when measuring the signals of ^{31}P nuclear in order to improve the signal-to-noise ratio. The whole duration of the evolution is 19ms whereas the decoherence time is of $\approx 44\text{ms}$. The decay of the signal caused by the decoherence is thus not negligible. We approximately compensate the decay by calibrating the signal of $\mathcal{L}_\delta^\Delta$ with that of $\mathcal{L}_0^\Delta \equiv \sum_{j=1}^{10} \gamma_j \text{Tr} \left(V_0(\vec{\theta}) \rho_{\text{eq}}^\Delta V_0^\dagger(\vec{\theta}) \sigma_z^j \right)$ (see Supplementary Material for details).

With the signal from the Loschmidt echo a classical optimization algorithm, the Nelder–Mead algorithm [35], is then used to update the parameters, $\vec{\theta}$, in the variational quantum circuit. The Nelder–Mead algorithm is a gradient-free optimization method which can be incorporated in the experiment easily. We also modified the algorithm to further improve its efficiency [36] (see Supplementary Material for detail).

The experimental results are shown in Fig. 3(a), where the blue triangles depicts the measured $\mathcal{L}_\delta^\Delta$ in experiment. It can be seen that the signal drops quickly at the beginning and tends to convergent with the increase of iterations, where the maximal number of iterations is set as 70. The blue dashed line is the simulated signal of Loschmidt echo from numerics which provides a benchmark for the experimental accuracy. The relative error between the experiment and the simulation is of 1.35%, this is mainly due to the relaxation as analyzed in Supplementary Material. The QFI obtained via Eq. (5) from the experiment data is depicted with the red stars, while the red dashed line is the theoretical QFI. The difference between them is mainly caused the neglect of higher-order terms in the correspondence of the Loschmidt echo and QFI at the finite value of δ . We also plot the optimal QFI [32] with the

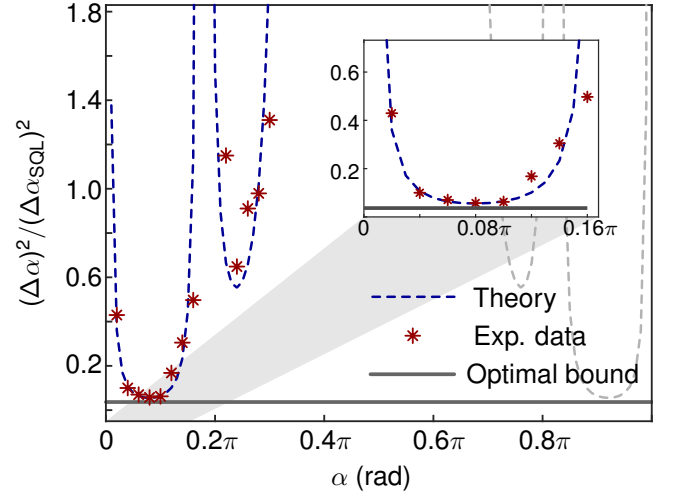


FIG. 4: The ratio of $\Delta\alpha$ in the ‘time-reversal-based readout’ protocol to the standard quantum limit (SQL). The red stars are obtained from experimental measurements, which outperforms the SQL with a factor of 12.4dB and conforms well with the theoretical blue dashed line. It’s more clear in the inset that though the ‘time-reversal-based readout’ protocol is not the optimal, a precision close to the optimal QCRB can still be realized with current engineered probe.

black solid line. Despite the presence of experimental imperfections, the prepared probe state via the variational quantum circuit is still near-optimal. We further characterize the generated ρ_f under 200 measurements and reconstruct the density matrix (see Supplemental Material for details). Utilizing the star-symmetry of the spin system, a brief representation of the reconstructed derivation density matrix ρ_f^Δ in the decomposed Hilbert space [37, 38] is shown on the right of Fig. 3(b). In contrast to ρ_{eq}^Δ on the left, the optimized state shows more population on the anti-diagonal positions of density matrix, thus achieving a faster phase accumulation. The QFI of the reconstructed ρ_f^Δ obtained from numerical calculation is $888\epsilon^2$, and it’s close to the theoretical value $951\epsilon^2$ and the optimum $952\epsilon^2$.

Phase estimation—After the optimization of the circuit, we then employ it for a typical application of quantum metrology, namely quantum phase estimation [39–43]. To further improve the sensitivity, at the measurement stage we replace the Loschmidt echo with a slightly different measurement (note that the Loschmidt echo is employed at the training stage). Given a measurement observable \mathcal{M} , the precision can be obtained with the error propagation formula [4]

$$(\Delta\alpha)^2 = \frac{(\Delta\mathcal{M})^2}{(d\langle\mathcal{M}\rangle/d\alpha)^2}, \quad (8)$$

where $\langle\mathcal{M}\rangle = \text{Tr}(\rho_f^\alpha \mathcal{M})$ and ρ_f^α is the encoded probe state. When \mathcal{M} is optimal, the precision saturates the QCRB quantified by the QFI. The optimal measurement, however, can be highly nontrivial which makes its implementation practically challenging. In the experiment we adopt an easy im-

plementing measurement protocol called 'time-reversal-based readout' protocol [44–46]. Similar with LE, it's obtained from the projection of encoded probe onto the engineered quantum state, i.e., $\text{Tr}(\rho_f^\alpha \rho_f)$. We experimentally characterize the attainable precision bound $(\Delta\alpha)^2$ by measuring $\langle \mathcal{M} \rangle$ and $\langle \mathcal{M}^2 \rangle$, in which $(\Delta\mathcal{M})^2$ is obtained from $\langle \mathcal{M}^2 \rangle - \langle \mathcal{M} \rangle^2$ and $d\langle \mathcal{M} \rangle/d\alpha$ is approximated by the difference method, i.e., $(\langle \mathcal{M} \rangle|_{\alpha+\delta'} - \langle \mathcal{M} \rangle|_{\alpha-\delta'})/2\delta'$ with δ' as a small shift and set as $\pi/50$ in the experiment. Details of this protocol are given in Supplementary Material, in which we also show this protocol achieves a precision with the Heisenberg scaling.

In Fig. 4, the experimental ratio of the precision under the 'time-reversal-based readout' protocol to the standard quantum limit (SQL) [47] is depicted with red stars, and it conforms well with the theoretical blue dashed line. The best precision occurs around $\bar{\alpha} = 0.08\pi$ with $(\Delta\alpha)^2/(\Delta\alpha_{\text{SQL}})^2 = 0.056$, which corresponds to the experimental precision $\Delta\alpha \approx 1.60 \times 10^{-3}$ and amounts to outperforming the SQL with a factor of 12.4 dB (details of experimental procedures can be seen in Supplementary Material). In practical implementation, we can always shift the α around $\bar{\alpha}$ with an additional field according to the adaptive method. We also plot the QCRB with the black solid line [32]. It's more clear in the inset that though the 'time-reversal-based readout' protocol is suboptimal, a quantum-enhanced precision close to the QCRB can still be realized with current engineered probe.

Conclusion—The present work has demonstrated the engineering of the optimal probe state with 10-spin NMR quantum computer. Quantum Fisher information, which quantifies the efficacy of engineered probe, is efficiently estimated by means of LE to guide the variational optimization. The experimental results of optimization indicates the engineered probe is close to the optimal one. Using the proposed 'time-reversal-based readout' protocol, a precision that close to the optimal QCRB can be achieved with the engineered probe. Our scheme is scalable, robust to experimental imperfections and easy to implement, which provides a promising routine to achieve quantum enhanced precisions on various noisy intermediate-scale quantum devices.

This work is supported by National Key R&D Program of China (Grant No. 2018YFA0306600), the National Natural Science Foundation of China (Grants Nos. 11661161018, 11927811, 12004371), Anhui Initiative in Quantum Information Technologies (Grant No. AHY050000), the Innovation Program for Quantum Science and Technology (Grant No. 2021ZD0303205), Research Grants Council of Hong Kong (GRF No. 14308019), and the Research Strategic Funding Scheme of The Chinese University of Hong Kong (No. 3133234).

* Electronic address: hdyan@mae.cuhk.edu.hk

† Electronic address: xhpeng@ustc.edu.cn

[1] A. S. Holevo, *Probabilistic and statistical aspects of quantum*

theory, Vol. 1 (Springer Science & Business Media, 2011).

- [2] C. W. Helstrom, *Journal of Statistical Physics* **1**, 231 (1969).
- [3] S. L. Braunstein and C. M. Caves, *Phys. Rev. Lett.* **72**, 3439 (1994).
- [4] V. Giovannetti, S. Lloyd, and L. Maccone, *Nature Photonics* **5**, 222 (2011).
- [5] V. Giovannetti, S. Lloyd, and L. Maccone, *Phys Rev Lett* **96**, 010401 (2006).
- [6] V. Giovannetti, S. Lloyd, and L. Maccone, *Science* **306**, 1330 (2004).
- [7] C. L. Degen, F. Reinhard, and P. Cappellaro, *Reviews of Modern Physics* **89**, 035002 (2017).
- [8] X. M. Lu, S. Yu, and C. H. Oh, *Nat Commun* **6**, 7282 (2015).
- [9] R. Demkowicz-Dobrzanski, J. Kolodynski, and M. Guta, *Nat Commun* **3**, 1063 (2012).
- [10] E. M. Kessler, I. Lovchinsky, A. O. Sushkov, and M. D. Lukin, *Phys Rev Lett* **112**, 150802 (2014).
- [11] R. Demkowicz-Dobrzanski and L. Maccone, *Phys Rev Lett* **113**, 250801 (2014).
- [12] C. D. Marciniak, T. Feldker, I. Pogorelov, R. Kaubruegger, D. V. Vasilyev, R. van Bijnen, P. Schindler, P. Zoller, R. Blatt, and T. Monz, *Nature* **603**, 604 (2022).
- [13] B. Koczor, S. Endo, T. Jones, Y. Matsuzaki, and S. C. Benjamin, *New Journal of Physics* **22**, 083038 (2020).
- [14] H. Xu, J. Li, L. Liu, Y. Wang, H. Yuan, and X. Wang, *npj Quantum Information* **5**, 82 (2019).
- [15] R. Kaubruegger, P. Silvi, C. Kokail, R. van Bijnen, A. M. Rey, J. Ye, A. M. Kaufman, and P. Zoller, *Physical Review Letters* **123**, 260505 (2019).
- [16] R. Kaubruegger, D. V. Vasilyev, M. Schulte, K. Hammerer, and P. Zoller, *Physical Review X* **11**, 041045 (2021).
- [17] H. Yuan and C. H. Fung, *Phys Rev Lett* **115**, 110401 (2015).
- [18] X. Yang, J. Thompson, Z. Wu, M. Gu, X. Peng, and J. Du, *npj Quantum Information* **6**, 62 (2020).
- [19] M. A. Nielsen and I. Chuang, *Quantum computation and quantum information* (2002).
- [20] P. Hauke, M. Heyl, L. Tagliacozzo, and P. Zoller, *Nature Physics* **12**, 778 (2016).
- [21] M. Garttner, P. Hauke, and A. M. Rey, *Phys Rev Lett* **120**, 040402 (2018).
- [22] A. Rath, C. Branciard, A. Minguzzi, and B. Vermersch, *Phys Rev Lett* **127**, 260501 (2021).
- [23] M. Yu, D. Li, J. Wang, Y. Chu, P. Yang, M. Gong, N. Goldman, and J. Cai, *Physical Review Research* **3**, 043122 (2021).
- [24] M. Cerezo, A. Sone, J. L. Beckey, and P. J. Coles, *Quantum Science and Technology* **6**, 035008 (2021).
- [25] K. Modi, L. C. Céleri, J. Thompson, and M. Gu, arXiv preprint arXiv:1608.01443 (2016).
- [26] J. L. Beckey, M. Cerezo, A. Sone, and P. J. Coles, *Physical Review Research* **4**, 013083 (2022).
- [27] S. L. Braunstein, C. M. Caves, and G. J. Milburn, *Annals of Physics* **247**, 135 (1996).
- [28] T. Gorin, T. Prosen, T. H. Seligman, and M. Žnidarič, *Physics Reports* **435**, 33 (2006).
- [29] A. Goussev, R. A. Jalabert, H. M. Pastawski, and D. Wisniacki, arXiv preprint arXiv:1206.6348 (2012).
- [30] T. Macrì, A. Smerzi, and L. Pezzè, *Physical Review A* **94**, 010102 (2016).
- [31] M. H. Levitt, *Spin dynamics: basics of nuclear magnetic resonance* (John Wiley & Sons, 2013).
- [32] L. J. Fiderer, J. M. E. Fraise, and D. Braun, *Phys Rev Lett* **123**, 250502 (2019).
- [33] L. M. K. Vandersypen and I. L. Chuang, *Reviews of Modern Physics* **76**, 1037 (2005).

- [34] A. J. Shaka, J. Keeler, and R. Freeman, *Journal of Magnetic Resonance* (1969) **53**, 313 (1983).
- [35] J. A. Nelder and R. Mead, *The Computer Journal* **7**, 308 (1965).
- [36] W. Spendley, G. R. Hext, and F. R. Himsworth, *Technometrics* **4**, 441 (1962).
- [37] J. Chen, Y. Zhou, J. Bian, J. Li, and X. Peng, *Physical Review A* **102**, 032602 (2020).
- [38] R. Liu, Y. Hou, Z. Wu, H. Zhou, J. Chen, X. Chen, Z. Li, and X. Peng, arXiv preprint arXiv:2206.08581 (2022).
- [39] P. M. Anisimov, G. M. Raterman, A. Chiruvelli, W. N. Plick, S. D. Huver, H. Lee, and J. P. Dowling, *Phys Rev Lett* **104**, 103602 (2010).
- [40] J. Joo, W. J. Munro, and T. P. Spiller, *Phys Rev Lett* **107**, 083601 (2011).
- [41] B. L. Higgins, D. W. Berry, S. D. Bartlett, H. M. Wiseman, and G. J. Pryde, *Nature* **450**, 393 (2007).
- [42] C. Schäfermeier, M. Ježek, L. S. Madsen, T. Gehring, and U. L. Andersen, *Optica* **5**, 60 (2018).
- [43] C. Oh, C. Lee, C. Rockstuhl, H. Jeong, J. Kim, H. Nha, and S.-Y. Lee, *npj Quantum Information* **5**, 10 (2019).
- [44] S. Colombo, E. Pedrozo-Peñafiel, A. F. Adiyatullin, Z. Li, E. Mendez, C. Shu, and V. Vuletić, *Nature Physics* **18**, 925 (2022).
- [45] S. P. Nolan, S. S. Szigeti, and S. A. Haine, *Phys Rev Lett* **119**, 193601 (2017).
- [46] J. Li, R. Fan, H. Wang, B. Ye, B. Zeng, H. Zhai, X. Peng, and J. Du, *Physical Review X* **7**, 031011 (2017).
- [47] K. Modi, H. Cable, M. Williamson, and V. Vedral, *Physical Review X* **1**, 021022 (2011).

Variational Quantum Metrology with Loschmidt Echo: Supplemental Material

Ran Liu,^{1,2} Ze Wu,^{1,2} Xiaodong Yang,^{3,4,5} Yuchen Li,^{1,2} Hui Zhou,⁶ Yuquan Chen,^{1,2} Haidong Yuan,^{7,*} Xinhua Peng,^{1,2,8,†} and Jiangfeng Du^{1,2,8}

¹CAS Key Laboratory of Microscale Magnetic Resonance and School of Physical Sciences, University of Science and Technology of China, Hefei 230026, China

²CAS Center for Excellence in Quantum Information and Quantum Physics, University of Science and Technology of China, Hefei 230026, China

³Shenzhen Institute for Quantum Science and Engineering, Southern University of Science and Technology, Shenzhen, 518055, China

⁴International Quantum Academy, Shenzhen, 518055, China

⁵Guangdong Provincial Key Laboratory of Quantum Science and Engineering, Southern University of Science and Technology, Shenzhen, 518055, China

⁶School of Physics, Hefei University of Technology, Hefei, Anhui 230009, China

⁷Department of Mechanical and Automation Engineering,

The Chinese University of Hong Kong, Shatin, Hong Kong SAR, China

⁸Hefei National Laboratory, University of Science and Technology of China, Hefei 230088, China

(Dated: November 23, 2022)

THE CONNECTION BETWEEN LOSCHMIDT ECHO AND QUANTUM FISHER INFORMATION

For the pure initial probe state $|\Psi_0\rangle$, the Loschmidt echo (LE) under engineering operation U_E and encoding dynamics G can be expressed as

$$\mathcal{L}_\delta = |\langle \Psi_0 | U_E^\dagger e^{-i\delta G} U_E | \Psi_0 \rangle|^2. \quad (\text{S1})$$

By expanding Eq.(S1) with Taylor series around $\delta = 0$, we have

$$\begin{aligned} \mathcal{L}_\delta &= \langle \Psi_f | e^{-i\delta G} | \Psi_f \rangle \langle \Psi_f | e^{i\delta G} | \Psi_f \rangle \\ &= \left(1 - i\delta \langle G \rangle - \frac{\delta^2}{2} \langle G^2 \rangle + \frac{i\delta^3}{6} \langle G^3 \rangle \right) \left(1 + i\delta \langle G \rangle - \frac{\delta^2}{2} \langle G^2 \rangle - \frac{i\delta^3}{6} \langle G^3 \rangle \right) + O(\delta^4) \\ &= 1 - \delta^2 (\langle G^2 \rangle - \langle G \rangle^2) + O(\delta^4), \end{aligned} \quad (\text{S2})$$

where $\langle \cdot \rangle \equiv \langle \Psi_f | \cdot | \Psi_f \rangle$ and $|\Psi_f\rangle \equiv U_E |\Psi_0\rangle$. As the quantum Fisher information (QFI) for pure state is

$$\mathcal{F}(|\Psi_f\rangle) = 4 (\langle G^2 \rangle - \langle G \rangle^2), \quad (\text{S3})$$

we have [1]

$$\mathcal{F}(|\Psi_f\rangle) = \lim_{\delta \rightarrow 0} 4 \frac{1 - \mathcal{L}_\delta}{\delta^2}. \quad (\text{S4})$$

For the mixed engineered probe $\rho_f = U_E \rho_0 U_E^\dagger$ with the eigendecomposition $\sum_{i=1}^d \lambda_i |\psi_i\rangle \langle \psi_i|$ and d as the dimension of the Hilbert space, the LE can be computed as

$$\begin{aligned} \mathcal{L}_\delta &= \text{Tr} (\rho_f e^{-i\delta G} \rho_f e^{i\delta G}) \\ &= \text{Tr} \left(\sum_{i=1} \lambda_i |\psi_i\rangle \langle \psi_i| e^{-i\delta G} \sum_{j=1} \lambda_j |\psi_j\rangle \langle \psi_j| e^{i\delta G} \right) \\ &= \sum_k \langle \psi_k | \sum_{i=1} \lambda_i |\psi_i\rangle \langle \psi_i| e^{-i\delta G} \sum_{j=1} \lambda_j |\psi_j\rangle \langle \psi_j| e^{i\delta G} | \psi_k \rangle \\ &= \sum_i \lambda_i^2 - \delta^2 \left(\sum_{i,j} \lambda_i \lambda_j |\langle \psi_i | G | \psi_j \rangle|^2 + \sum_i \lambda_i^2 \langle \psi_i | G^2 | \psi_i \rangle \right) + O(\delta^4) \end{aligned} \quad (\text{S5})$$

The zero-order term in the perturbation expansion, i.e., $\sum_i \lambda_i^2$, represents the purity of ρ_0 , and it doesn't change under unitary transformation. While for the second-order terms, note that

$$\begin{aligned} \sum_i \lambda_i^2 \langle \psi_i | G^2 | \psi_i \rangle &= \frac{1}{2} \left(\sum_i \lambda_i^2 \langle \psi_i | G^2 | \psi_i \rangle + \sum_j \lambda_j^2 \langle \psi_j | G^2 | \psi_j \rangle \right) \\ \langle \psi_i | G^2 | \psi_i \rangle &= \langle \psi_i | G \sum_j |\psi_j\rangle \langle \psi_j | G | \psi_i \rangle = \sum_j |\langle \psi_i | G | \psi_j \rangle|^2, \end{aligned} \quad (\text{S6})$$

we thus have

$$\begin{aligned} \mathcal{L}_\delta &= \sum_i \lambda_i^2 + \sum_{i,j} \lambda_i \lambda_j \delta^2 |\langle \psi_i | G | \psi_j \rangle|^2 - \frac{\delta^2}{2} \sum_{i,j} \lambda_i^2 \delta^2 |\langle \psi_i | G | \psi_j \rangle|^2 - \frac{\delta^2}{2} \sum_{i,j} \lambda_j^2 \delta^2 |\langle \psi_i | G | \psi_j \rangle|^2 + O(\delta^4) \\ &= \sum_i \lambda_i^2 - \frac{\delta^2}{4} \left(2 \sum_{i,j} (\lambda_i - \lambda_j)^2 |\langle \psi_i | G | \psi_j \rangle|^2 \right) + O(\delta^4). \end{aligned} \quad (\text{S7})$$

Comparing with the QFI for mixed states

$$\mathcal{F}(\rho_f) = 2 \sum_{i,j} \frac{(\lambda_i - \lambda_j)^2}{\lambda_i + \lambda_j} |\langle \psi_i | G | \psi_j \rangle|^2, \quad (\text{S8})$$

we have

$$\mathcal{F}(\rho_f) \geq \lim_{\delta \rightarrow 0} 4 \frac{\gamma(\rho_f) - \mathcal{L}_\delta}{\delta^2}, \quad (\text{S9})$$

where we used the fact that $\lambda_i + \lambda_j \leq 1$, and $\gamma(\cdot)$ is the purity of the state. For highly mixed states where the eigenvalues are almost degenerate, i.e., $\lambda_i \approx \frac{1}{d}$ for $1 \leq i \leq d$, we have

$$\mathcal{F}(\rho_f) \approx \lim_{\delta \rightarrow 0} 2d \frac{\gamma(\rho_f) - \mathcal{L}_\delta}{\delta^2}, \quad (\text{S10})$$

OPTIMAL QUENCH TIME UNDER ENCODING DYNAMICS

When extracting QFI from LE according to Eq. (S10), there are three factors that can lead to the deviation from the theoretical QFI: 1) the eigenvalues of ρ_f are not exactly equal to $1/d$; 2) the higher (>2) order terms are ignored in Eq. (S10) but they can be non-zero; 3) the experimental errors when measuring the LE. In the following, we give an analysis on how these factors affect the deviation and decide an optimal value of δ for the experimental extraction of the QFI from Eq. (S10).

- 1) In our experiments, the equilibrium state is $\rho_0 = (\mathbb{1} + \epsilon \rho_0^\Delta) / 2^N$ with $\rho_0^\Delta = \gamma_P \sigma_z^P + \gamma_H \sum_{j=1}^9 \sigma_{j,z}^H$. The eigenvalues can then be expressed as $\lambda_i = 1/2^N + \lambda_i^\Delta$ with $\lambda_i^\Delta \sim N\epsilon/2^N$. The error caused by taking λ_i as $1/d = 1/2^N$ can thus be obtained as

$$\begin{aligned} \mathcal{E}_1 &= 2 \sum_{i,j} (\lambda_i - \lambda_j)^2 |\langle \psi_i | G | \psi_j \rangle|^2 \left| \frac{1}{2^N} - \frac{1}{\frac{2}{2^N} + \lambda_i^\Delta + \lambda_j^\Delta} \right| \\ &= 2 \sum_{i,j} (\lambda_i^\Delta - \lambda_j^\Delta)^2 |\langle \psi_i | G | \psi_j \rangle|^2 \left| \frac{\lambda_i^\Delta + \lambda_j^\Delta}{\frac{2}{2^N} (\frac{2}{2^N} + \lambda_i^\Delta + \lambda_j^\Delta)} \right| \\ &\sim \frac{(N\epsilon)^3}{2^{N+2}} \end{aligned} \quad (\text{S11})$$

- 2) For the Taylor series expansion of \mathcal{L}_δ , its higher-order terms are non-negligible under finite δ . The leading term, i.e., the fourth-order term, is

$$\delta^4 \left(\frac{1}{4} \sum_{i,j} \lambda_i \lambda_j |\langle \psi_i | G^2 | \psi_j \rangle|^2 + \frac{1}{12} \sum_i \lambda_i^2 \langle \psi_j | G^4 | \psi_i \rangle - \frac{1}{3} \sum_{i,j} \lambda_i \lambda_j \text{real} (\langle \psi_j | G | \psi_i \rangle \langle \psi_i | G^3 | \psi_j \rangle) \right). \quad (\text{S12})$$

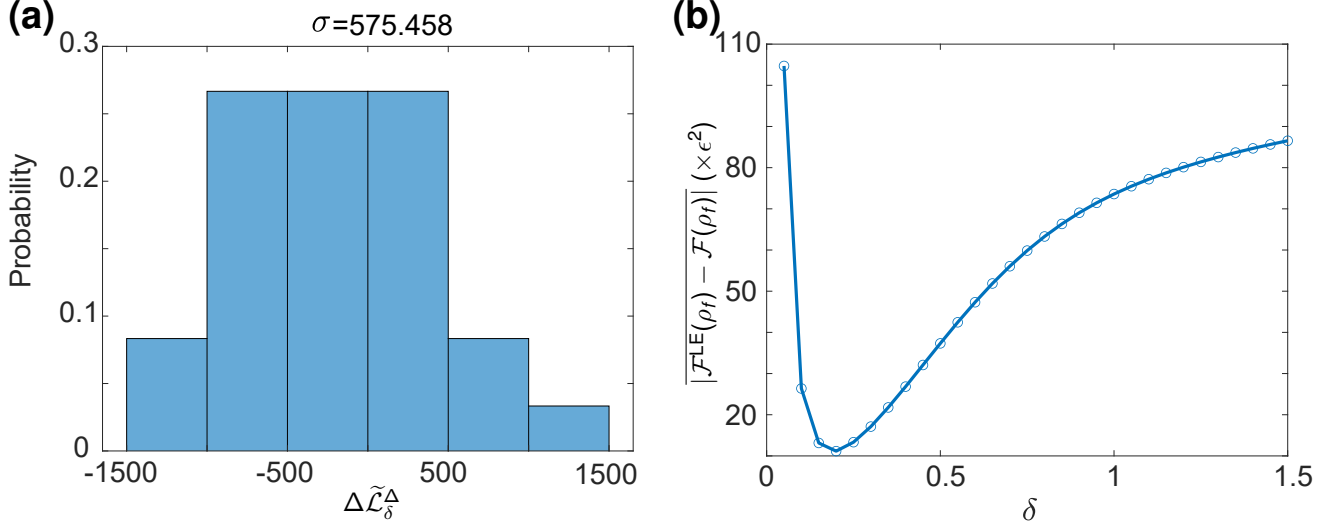


FIG. S1: (a) Calibration of experimental error for measuring $\mathcal{L}_\delta^\Delta$. (b) Numerical simulation of error of QFI under different quench time δ . When $\delta = 0.2$, the error gets its minimum.

Consequently, it leads to the error on QFI

$$\mathcal{E}_2 \sim \frac{\delta^2}{2^{N-1}}. \quad (\text{S13})$$

- 3) As we mentioned in the main text, \mathcal{L}_δ is experimentally obtained by measuring its deviation part $\mathcal{L}_\delta^\Delta$, i.e., $\mathcal{L}_\delta = 1/2^N + \epsilon^2 \mathcal{L}_\delta^\Delta$. The deviations of the experimental results $\mathcal{L}_\delta^{\Delta, \text{exp}}$ from the theoretical one leads to the error on QFI,

$$\mathcal{E}_3 \sim \frac{2^{N+1} \epsilon^2 \Delta \mathcal{L}_\delta^\Delta}{\delta^2} \quad (\text{S14})$$

with $\Delta \mathcal{L}_\delta^\Delta = \mathcal{L}_\delta^{\Delta, \text{exp}} - \mathcal{L}_\delta^{\Delta, \text{theo}}$. We calibrate the deviations from experiments by measuring $\mathcal{L}_\delta^{\Delta, \text{exp}}$ under 80 different $U_E(\theta)$ and calculating their standard deviation as $\sigma = 575.46$. The probability histogram is shown in Fig. S1 (a).

Since $\epsilon \sim 10^{-5}$ at the thermal polarization, \mathcal{E}_1 is much smaller than \mathcal{E}_2 and \mathcal{E}_3 , thus negligible. The influences of δ on \mathcal{E}_2 and \mathcal{E}_3 are opposite, as Eq.(S13) shows \mathcal{E}_2 increases with δ while Eq.(S14) shows \mathcal{E}_3 decreases with δ . Thus there exists a tradeoff and an optimal δ needs to be determined to minimize the total error. As shown in Fig. S1 (b), we numerically simulate the mean of the difference between the QFI obtained from the LE under experimental errors and the theoretical one, i.e., $|\overline{\mathcal{F}^{\text{LE}}(\rho_f)} - \mathcal{F}(\rho_f)|$, under 50 different $U_E(\theta)$ for each δ . The experimental error is simulated by adding artificial fluctuations on $\mathcal{L}_\delta^\Delta$ obeying normal distribution with a standard deviation σ . From the simulation we can see that the error is minimal at $\delta = 0.2$, which is taken as the experimental quench time.

DETAILS OF THE NELDER-MEAD ALGORITHM

The Nelder-Mead algorithm provides a useful procedure for searching the minimum of a given function without derivatives. By rescaling a simplex consisting of $n + 1$ vertices iteratively, this algorithm attempts to replace the worst vertex by a better one. Here each vertex represents a sequence of n parameters that can be tuned in the parametrized quantum circuit(PQC). The procedure of the Nelder-Mead algorithm is described as below.

1. **Ordering:** Calculate the cost function of $n + 1$ initial vertices and sort them as

$$f(\theta^{(1)}) \leq f(\theta^{(2)}) \leq \dots \leq f(\theta^{(n+1)}). \quad (\text{S15})$$

where the cost function is LE with $f(\theta^{(i)}) = \mathcal{L}_\delta(\theta^{(i)})$. For the 3-layer PQC used in the experiment we have $n = 6$.

2. **Centroid:** Evaluate the cost function of the centroid of the best n points, $f(\boldsymbol{\theta}^{\text{ave}})$, here $\boldsymbol{\theta}^{\text{ave}} = \sum_{i=1}^n \boldsymbol{\theta}^{(i)}/n$.
3. **transformation:** Replace the worst vertex $\boldsymbol{\theta}^{(n+1)}$ and the corresponding cost function with a better one by using reflection, expansion, contraction or shrink. The concrete rules for this transformation are as follows:
 - (1) **Reflect:** Calculate the cost function of $f_r = f(\boldsymbol{\theta}^r)$ with $\boldsymbol{\theta}^r := \boldsymbol{\theta}^{\text{ave}} + \alpha(\boldsymbol{\theta}^{(n+1)} - \boldsymbol{\theta}^{(n)})$ as the reflection point. α is the reflection coefficient and set as 1. If $f_1 \leq f_r \leq f_n$, accept $\boldsymbol{\theta}^r$.
 - (2) **Expand:** If $f_r < f_1$, calculate $f_e = f(\boldsymbol{\theta}^e)$ with $\boldsymbol{\theta}^e := \boldsymbol{\theta}^{\text{ave}} + \gamma \cdot \alpha(\boldsymbol{\theta}^{(n+1)} - \boldsymbol{\theta}^{(n)})$ as the expansion point and γ is the expansion coefficient and set as 2. If $f_e < f_r$ accept $\boldsymbol{\theta}^e$. Otherwise, accept $\boldsymbol{\theta}^r$.
 - (3) **Contract:** (3a) If $f_n \leq f_r \leq f_{n+1}$, calculate $f_c := f(\boldsymbol{\theta}^c)$ with $\boldsymbol{\theta}^c := \boldsymbol{\theta}^{\text{ave}} + \beta \cdot \alpha(\boldsymbol{\theta}^{(n+1)} - \boldsymbol{\theta}^{(n)})$ as the outside contraction point and β is the contraction coefficient and set as 0.5. If $f_c \leq f_r$, accept f_c . Otherwise, perform a shrink transformation. (3b) If $f_r \geq f_{n+1}$, calculate $f_c := f(\boldsymbol{\theta}^c)$ with $\boldsymbol{\theta}^c := \boldsymbol{\theta}^{\text{ave}} - \beta \cdot \alpha(\boldsymbol{\theta}^{(n+1)} - \boldsymbol{\theta}^{(n)})$ as the inside contraction point and β is set as 0.5. If $f_c \leq f_r$, accept f_c . Otherwise, perform a shrink transformation.
- (4) **Shrink:** Calculate $f_i := f(\boldsymbol{\theta}^{(i)})$ with $\boldsymbol{\theta}^{(i)} := \boldsymbol{\theta}^{(1)} + (1 - \delta)\boldsymbol{\theta}^{(i)}$ and $i = 2, 3, \dots, n+1$. δ is the shrinkage coefficient and set as 0.5.
4. **Termination tests:** If the result satisfies the stopping condition, terminate the iterations. Otherwise, change the iteration number as $l = l + 1$ and continue at **Ordering**.

Here the stopping condition is whether the optimized QFI is close to the optimum. We simulate 30 rounds of experimental iterations, and in each round the initial vertices ($l = 1$) is generated randomly with $\boldsymbol{\theta}_i \in [0, 2\pi]$ and $i = 1, 2, \dots, n+1$. To take the experimental errors into account, we add fluctuations on theoretical $\mathcal{L}_\delta^\Delta$ with the standard deviation σ as obtained in Sec. . The simulated result in Fig. S2 (a) shows that the optimization converges and approaches to its optimum when $l \geq 70$. Consequently, we stop the experimental iterations when $l = 70$.

To improve the efficiency of the optimization, we further modify the initial simplex ($l = 1$) as [2]

$$\boldsymbol{\theta}_j^{(i)} = \begin{cases} \boldsymbol{\theta}_j^{(1)} + 2\pi(\sqrt{n+1} - 1) & i \neq j + 1 \& i > 1 \\ \boldsymbol{\theta}_j^{(1)} + 2\pi(\sqrt{n+1} + n - 1) & i = j + 1 \& i > 1 \end{cases} \quad (\text{S16})$$

and $\boldsymbol{\theta}^{(1)} = (0, 0, \dots, 0)^T$. We simulate 100 rounds of optimization under this initial simplex and stop the iteration when $l = 70$. The statistical result of optimized QFI is show in Fig. S2 (b). Compared with the case of randomly generated initial simplex, as shown in Fig. S2 (c)-(k), the modified one shows higher expectation to approach a large QFI under noise, thus adopted in the experiment.

STRUCTURE OF PARAMETERIZED QUANTUM CIRCUIT AND ITS REACHABLE SET

The structure of PQC used to realize the engineering operation U_E is shown in Fig. S3. The PQC has 3 layers with the first layer being local rotations along y -axis while the others consisting of an entangling gate and local rotations. The entangling gate is realized by the free evolution under the system Hamiltonian $H_{\text{NMR}} = \frac{\pi}{2} J_{\text{PH}} \sigma_z^1 \otimes \sum_{j=2}^{10} \sigma_z^j$ with the interval $\tau = 1/2J_{\text{PH}}$, and the parameters are the angles of local rotation $\boldsymbol{\theta} := (\theta_1, \theta_2, \dots, \theta_6)^T$. We now show that the reachable set of quantum state generated by $U_E(\boldsymbol{\theta})$, denote as \mathcal{R}_{U_E} , includes the optimal probe state.

The polarized part of initial equilibrium state can be written as $\gamma_{\text{P}} Z(I^{\otimes 9})/9 + \gamma_{\text{H}} I(ZI^{\otimes 8})$, here X, Y, Z, I represent $\sigma_{x,y,z}, \mathbb{1}_2$ respectively, and (\cdot) represent the summation over all the indistinguishable permutations, such as $(I^{\otimes 9}) := \sum_{i=1}^9 I^{\otimes 9} \dots$, $(ZI^{\otimes 8}) := ZII \dots + IZI \dots + IIZ \dots + \dots$. The evolved state after $e^{-i(\theta_1 \sigma_y/2 + \theta_4 \sum_{j=2}^{10} \sigma_y^j/2)}$, corresponding to stage ① in Fig. S3, is

$$\begin{aligned} \textcircled{1} : Z(I^{\otimes 9}) &\rightarrow \cos \theta_1 Z(I^{\otimes 9}) + \sin \theta_1 X(I^{\otimes 9}) \\ I(ZI^{\otimes 8}) &\rightarrow \cos \theta_4 I(ZI^{\otimes 8}) + \sin \theta_4 I(XI^{\otimes 8}) \\ \rho_{\textcircled{1}} &= \gamma_{\text{P}} [\cos \theta_1 Z(I^{\otimes 9}) + \sin \theta_1 X(I^{\otimes 9})] / 9 + \gamma_{\text{H}} [\cos \theta_4 I(ZI^{\otimes 8}) + \sin \theta_4 I(XI^{\otimes 8})] \end{aligned} \quad (\text{S17})$$

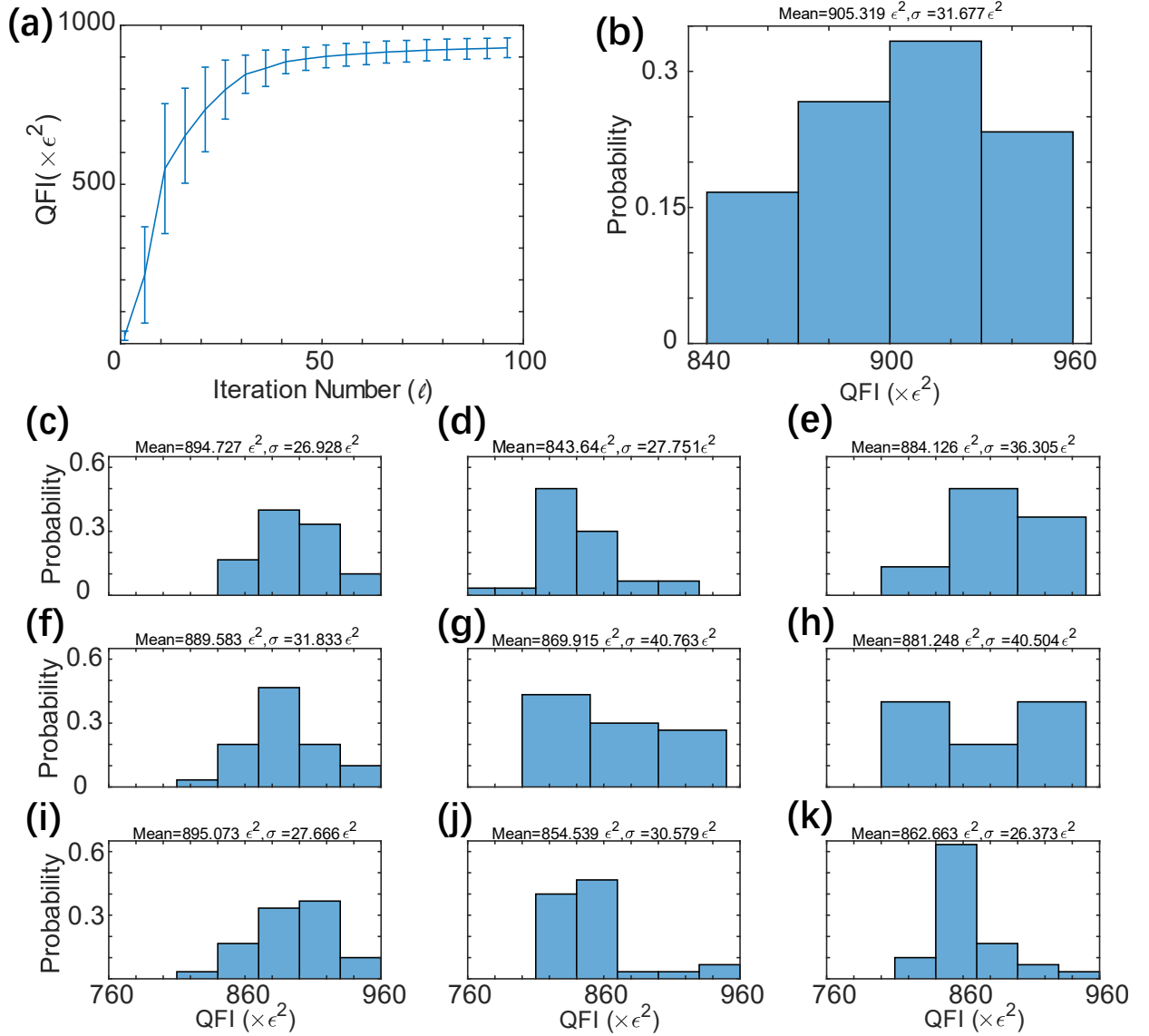


FIG. S2: Simulated iterations with NM algorithm. (a) Statistical result of 30 rounds of iteration under different initial simplexes and random fluctuation. When $\ell \geq 70$, the optimization converges and approaches to its optimum. Statistical result of optimized QFI obtained from 100 rounds of iteration with (b) modified initial simplex and (c-k) random initial simplex. The modified one shows higher expectation to approach a large QFI.

Since $[\sigma_z^1 \sigma_z^i, \sigma_z^1 \sigma_z^j] = 0$ for $i, j = 1, 2, \dots, 9$, the different terms in H_{NMR} can then be applied in turn,

$$\begin{aligned}
 \textcircled{2} : & Z(I^{\otimes 9}) \rightarrow Z(I^{\otimes 9}) \\
 & X(I^{\otimes 9}) \xrightarrow{I_z^0 I_z^1} 9YZI^{\otimes 8} \xrightarrow{I_z^0 I_z^2} -9XZZI^{\otimes 7} \xrightarrow{I_z^0 I_z^3} \dots \xrightarrow{I_z^0 I_z^9} Y(Z^{\otimes 9}) \\
 & I(ZI^{\otimes 8}) \rightarrow I(ZI^{\otimes 8}) \\
 & I(XI^{\otimes 8}) \rightarrow Z(YI^{\otimes 8}) \\
 \rho_{\textcircled{2}} = & \gamma_{\text{P}} [\cos \theta_1 Z(I^{\otimes 9}) + \sin \theta_1 Y(Z^{\otimes 9})] / 9 + \gamma_{\text{H}} [\cos \theta_4 I(ZI^{\otimes 8}) + \sin \theta_4 Z(YI^{\otimes 8})].
 \end{aligned} \tag{S18}$$

Similarly, we have

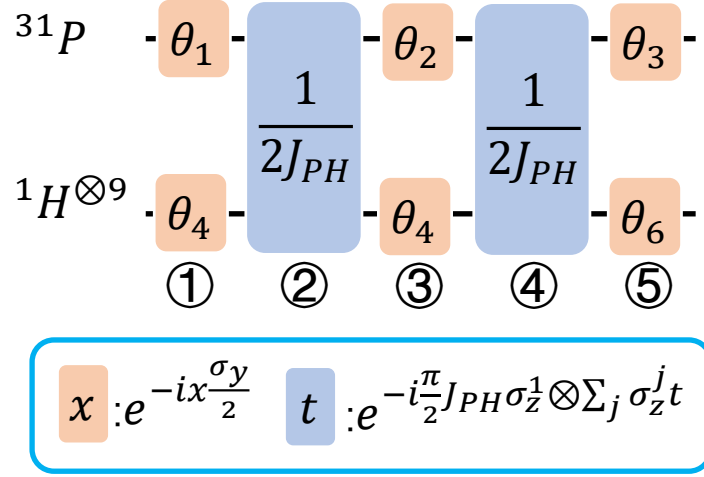


FIG. S3: The structure of PQC used to engineer quantum probe, which consists of single-qubit rotations and entangling gates. Its reachable set of quantum states can cover the optimal quantum probe when $\sin \theta_2 = 1, \sin \theta_6 = 1, \cos \theta_1 \cos \theta_3 \sin \theta_4 = 1$.

$$\begin{aligned}
 \textcircled{3} : Z(I^{\otimes 9}) &\rightarrow \cos \theta_2 Z(I^{\otimes 9}) + \sin \theta_2 X(I^{\otimes 9}) \\
 Y(Z^{\otimes 9}) &\rightarrow \sum_{i=1}^{10} \cos^{10-i} \theta_5 \sin^{i-1} \theta_5 Y(Z^{\otimes 10-i} X^{\otimes i-1}) \\
 I(ZI^{\otimes 8}) &\rightarrow \cos \theta_5 I(ZI^{\otimes 8}) + \sin \theta_5 I(XI^{\otimes 8}) \\
 Z(YI^{\otimes 8}) &\rightarrow \cos \theta_2 Z(YI^{\otimes 8}) + \sin \theta_2 X(YI^{\otimes 8}) \\
 \rho_{\textcircled{3}} &= \gamma_P \left[\cos \theta_1 (\cos \theta_2 Z(I^{\otimes 9}) + \sin \theta_2 X(I^{\otimes 9})) + \sin \theta_1 \left(\sum_{i=1}^{10} \cos^{10-i} \theta_5 \sin^{i-1} \theta_5 Y(Z^{\otimes 10-i} X^{\otimes i-1}) \right) \right] / 9 \\
 &+ \gamma_H [\cos \theta_4 (\cos \theta_5 I(ZI^{\otimes 8}) + \sin \theta_5 I(XI^{\otimes 8})) + \sin \theta_4 (\cos \theta_2 Z(YI^{\otimes 8}) + \sin \theta_2 X(YI^{\otimes 8}))]
 \end{aligned} \tag{S19}$$

$$\begin{aligned}
 \textcircled{4} : Z(I^{\otimes 9}) &\rightarrow Z(I^{\otimes 9}) \\
 X(I^{\otimes 9}) &\rightarrow Y(Z^{\otimes 9}) \\
 Y(Z^{\otimes 9}) &\xrightarrow{I_z^1 I_z^2} -9XIZ^{\otimes 8} \xrightarrow{I_z^1 I_z^3} -9YIIZ^{\otimes 7} \xrightarrow{I_z^1 I_z^4} \dots \xrightarrow{I_z^1 I_z^{10}} X(I^{\otimes 9}) \\
 Y(XZ^{\otimes 8}) &\rightarrow Y(XI^{\otimes 8}) \\
 \text{due to } YXZ^{\otimes 8} &\xrightarrow{I_z^1 I_z^2} YXZ^{\otimes 8} \xrightarrow{I_z^1 I_z^3} XXIZ^{\otimes 7} \xrightarrow{I_z^1 I_z^4} \dots \xrightarrow{I_z^1 I_z^{10}} YXI^{\otimes 8} \\
 \dots & \\
 Y(ZX^{\otimes 8}) &\rightarrow X(IX^{\otimes 8}) \\
 \text{due to } YZX^{\otimes 8} &\xrightarrow{I_z^1 I_z^2} XIX^{\otimes 8} \xrightarrow{I_z^1 I_z^3} XIX^{\otimes 8} \xrightarrow{I_z^1 I_z^4} \dots \xrightarrow{I_z^1 I_z^{10}} XIX^{\otimes 8} \\
 Y(X^{\otimes 9}) &\rightarrow Y(X^{\otimes 9}) \\
 I(ZI^{\otimes 8}) &\rightarrow I(ZI^{\otimes 8}) \\
 I(XI^{\otimes 8}) &\rightarrow Z(YI^{\otimes 8}) \\
 Z(YI^{\otimes 8}) &\rightarrow I(XI^{\otimes 8}) \\
 X(YI^{\otimes 8}) &\rightarrow X(YZ^{\otimes 8}) \\
 \text{due to } XYI^{\otimes 8} &\xrightarrow{I_z^1 I_z^2} XYI^{\otimes 8} \xrightarrow{I_z^1 I_z^3} YYZI^{\otimes 7} \xrightarrow{I_z^1 I_z^4} \dots \xrightarrow{I_z^1 I_z^{10}} XYZ^{\otimes 8}
 \end{aligned} \tag{S20}$$

$$\rho_{\textcircled{4}} = \gamma_{\text{P}} \left[\cos \theta_1 (\cos \theta_2 Z(I^{\otimes 9}) + \sin \theta_2 Y(Z^{\otimes 9})) + \sin \theta_1 \sum_{i=1}^{10} \cos^{10-i} \theta_5 \sin^{i-1} \theta_5 (X \text{ or } Y)(I^{\otimes 10-i} X^{\otimes i-1}) \right] / 9 \quad (\text{S21})$$

$$+ \gamma_{\text{H}} [\cos \theta_4 (\cos \theta_5 I(ZI^{\otimes 8}) + \sin \theta_5 Z(YI^{\otimes 8})) + \sin \theta_4 (\cos \theta_2 I(XI^{\otimes 8}) + \sin \theta_2 X(YZ^{\otimes 8}))]$$

$$\textcircled{5} : Z(I^{\otimes 9}) \rightarrow \cos \theta_3 Z(I^{\otimes 9}) + \sin \theta_3 X(I^{\otimes 9})$$

$$Y(Z^{\otimes 9}) \rightarrow \sum_{i=1}^{10} \cos^{10-i} \theta_6 \sin^{i-1} \theta_6 Y(Z^{\otimes 10-i} X^{\otimes i-1})$$

$$X(I^{\otimes 9}) \rightarrow \cos \theta_3 X(I^{\otimes 9}) - \sin \theta_3 Z(I^{\otimes 9})$$

$$Y(XI^{\otimes 8}) \rightarrow \cos \theta_6 Y(XI^{\otimes 9}) - \sin \theta_6 Y(ZI^{\otimes 9})$$

$$\dots$$

$$X(IX^{\otimes 8}) \xrightarrow{\theta_3 I_y^1} \cos \theta_3 X(IX^{\otimes 8}) - \sin \theta_3 Z(IX^{\otimes 8})$$

$$\xrightarrow{\theta_6 \sum_i I_y^i} \cos \theta_3 \left(\sum_{i=1}^9 \cos^{9-i} \sin^{i-1} \theta_6 X(IX^{\otimes 9-i} Z^{\otimes i-1}) \right) - \sin \theta_3 \left(\sum_{i=1}^9 \cos^{9-i} \sin^{i-1} \theta_6 Z(IX^{\otimes 9-i} Z^{\otimes i-1}) \right) \quad (\text{S22})$$

$$Y(X^{\otimes 9}) \rightarrow \sum_{i=1}^{10} \cos^{10-i} \theta_6 (-\sin \theta_6)^{i-1} Y(X^{\otimes 10-i} Z^{\otimes i-1})$$

$$I(ZI^{\otimes 8}) \rightarrow \cos \theta_6 I(ZI^{\otimes 8}) + \sin \theta_6 I(XI^{\otimes 8})$$

$$Z(YI^{\otimes 8}) \rightarrow \cos \theta_3 Z(YI^{\otimes 8}) + \sin \theta_3 X(YI^{\otimes 8})$$

$$I(XI^{\otimes 8}) \rightarrow \cos \theta_6 I(XI^{\otimes 8}) - \sin \theta_6 I(ZI^{\otimes 8})$$

$$X(YZ^{\otimes 8}) \xrightarrow{\theta_3 I_y^1} \cos \theta_3 X(YZ^{\otimes 8}) - \sin \theta_3 Z(YZ^{\otimes 8})$$

$$\xrightarrow{\theta_6 \sum_i I_y^i} \cos \theta_3 \left(\sum_{i=1}^9 \cos^{9-i} \sin^{i-1} \theta_6 X(YZ^{\otimes 9-i} X^{\otimes i-1}) \right) - \sin \theta_3 \left(\sum_{i=1}^9 \cos^{9-i} \sin^{i-1} \theta_6 Z(YZ^{\otimes 9-i} X^{\otimes i-1}) \right)$$

Consequently, $\mathcal{R}_{U_{\text{E}}}$ can be given by $\textcircled{5}$ with $\theta_1, \theta_2, \dots, \theta_6 \in [0, 2\pi]$.

The optimal probe is given by Ref. [3]

$$\rho^* = \sum_{i=1}^d \lambda_i |\Phi_i^*\rangle \langle \Phi_i^*|, \quad (\text{S23})$$

with

$$|\Phi_i^*\rangle = \begin{cases} \frac{|\phi_i\rangle + |\phi_{d-i+1}\rangle}{\sqrt{2}} & \text{if } 2i < d+1, \\ |\phi_i\rangle & \text{if } 2i = d+1, \\ \frac{|\phi_i\rangle - |\phi_{d-i+1}\rangle}{\sqrt{2}} & \text{if } 2i > d+1. \end{cases} \quad (\text{S24})$$

This form guarantees the maximization of the amplitude of highest-order coherence, as the elements with higher-order coherence in probe state show faster phase accumulation. Under the encoding dynamics $G = \sum_{k=1}^{10} \sigma_z / 2$, X, Y contribute to the order of coherence while I, Z don't. In the following, we consider the highest-order, i.e., 10-order, coherence in probe,

$$\rho_{(10)}^{\Delta} = \frac{\gamma_{\text{P}}}{9} [\cos \theta_1 \sin \theta_2 \sin^9 \theta_6 Y(X^{\otimes 9}) + \sin \theta_1 \sin^9 \theta_5 \cos^9 \theta_6 Y(X^{\otimes 9})] + \gamma_{\text{H}} \sin \theta_4 \sin \theta_2 \cos \theta_3 \sin^8 \theta_6 X(YX^{\otimes 8}). \quad (\text{S25})$$

When $\sin \theta_2 = 1, \sin \theta_6 = 1, \cos \theta_1 \cos \theta_3 \sin \theta_4 = 1$, the contribution of $\rho_{(10)}^{\Delta}$ is maximized and the corresponding probe is optimal. So $\mathcal{R}_{U_{\text{E}}}$ can cover the optimal probe.

ANALYSIS OF EXPERIMENTAL ERRORS AND TECHNIQUES USED TO SUPPRESS THEM

As mentioned in the main text, the relative error of measured $\mathcal{L}_{\delta}^{\Delta}$ during the iteration is 1.35%. The sources of experimental errors include the pulse error, relaxation and measurement error. We employ different techniques to

TABLE S1: Analysis of the experimental errors and the experimental techniques employed to suppress the errors.

Total experimental error: 1.35%			
Sources of experimental error	Pulse error	Relaxation	Measurement error
Contributions (regular pulse sequence)	8.1%	8.2%	$2.5 \times 10^{-2}\%$
Contributions (specific experimental technique)	$4.5 \times 10^{-2}\%$ (BB1 sequence)	0.98% (calibration with \mathcal{L}_0^Δ)	$1.8 \times 10^{-2}\%$ (composite pulse decoupling)

suppress them. A detailed introduction of these techniques and the analysis of the experimental errors, aided with numerical simulations, are listed in the following.

- Pulse error:** The pulse error can lead to the deviation between the actually implemented rotation angles and the desired ones. This is mainly caused by the imperfect calibration of $\pi/2$ -pulse in NMR experiment. To improve the robustness of the pulses, we replace the regular pulses with the BB1 sequence $R_\phi(\theta) \rightarrow R_\phi(\pi)R_{3\phi}(2\pi)R_\phi(\pi)R_\phi(\theta)$, where θ and ϕ is the target angle and phase, $\phi = \arccos(-\theta/4\pi)$. We simulate the pulse error by adding random fluctuation with 5% relative distortions to the amplitude of the pulses. The result shows that the relative error of $\mathcal{L}_\delta^\Delta$ caused by the pulse error decreases from 8.1% to $4.5 \times 10^{-2}\%$ after applying the BB1 sequence. Thus the pulse error is significantly suppressed.
- Relaxation:** The quantum probe inevitably interacts with the environment during the evolution. The noise in NMR experiment can be described by the phase damping channel, \mathcal{E}_{PD} , and the generalized amplitude damping channel, \mathcal{E}_{GAD} . The effect of the phase damping channel on the density matrix ρ can be approximately expressed as $\rho \rightarrow \mathcal{E}_{\text{PD}}^N \circ \dots \circ \mathcal{E}_{\text{PD}}^2 \circ \mathcal{E}_{\text{PD}}^1(\rho)$, where $\mathcal{E}_{\text{PD}}^i(\rho) = (1 - \xi_i)\rho + \xi_i\sigma_z^i\rho\sigma_z^i$, $\xi_i = \frac{1}{2}[1 - \exp(-\Delta t/T_2^i)]$ with T_2^i as the transversal relaxation time of the i th spin. The influence of the generalized amplitude damping can be approximately characterized as $\rho \rightarrow \mathcal{E}_{\text{GAD}}^N \circ \dots \circ \mathcal{E}_{\text{GAD}}^2 \circ \mathcal{E}_{\text{GAD}}^1(\rho)$, where $\mathcal{E}_{\text{GAD}}^j(\rho) = \sum_s E_s^j \rho E_s^{j\dagger}$,

$$\begin{aligned}
 E_1^j &= \sqrt{\frac{1}{2}} \begin{pmatrix} 1 & 0 \\ 0 & \sqrt{1-\eta_j} \end{pmatrix}, & E_2^j &= \sqrt{\frac{1}{2}} \begin{pmatrix} 0 & 0 \\ \sqrt{\eta_j} & 0 \end{pmatrix}, \\
 E_3^j &= \sqrt{\frac{1}{2}} \begin{pmatrix} \sqrt{1-\eta_j} & 0 \\ 0 & 1 \end{pmatrix}, & E_4^j &= \sqrt{\frac{1}{2}} \begin{pmatrix} 0 & \sqrt{\eta_j} \\ 0 & 0 \end{pmatrix},
 \end{aligned} \tag{S26}$$

$\eta_j = 1 - \exp(-\Delta t/T_1^j)$ with T_1^j as the longitudinal relaxation time of the j th qubit. The relaxation time for ^{31}P nuclear spin and ^1H nuclear spins are $T_2^{\text{P}} = 1.30$ sec, $T_1^{\text{P}} = 5$ sec and $T_2^{\text{H}} = 1.26$ sec, $T_1^{\text{H}} = 4.2$ sec, respectively. Moreover, a main source of phase damping in NMR experiment is the inhomogeneity of static magnetic field, and we suppress this effect by employing the refocusing sequences during the free evolution. The evolution time in a single experiment is 187 msec, thus the effect of the relaxation is not negligible. The numerical results show that the relative error of $\mathcal{L}_\delta^\Delta$ caused by the relaxation is 8.2%. To compensate the decay of the signal, we calibrate the signal of $\mathcal{L}_\delta^\Delta$ with that of $\mathcal{L}_0^\Delta \equiv \sum_{j=1}^{10} \gamma_j \text{Tr}(V_0(\theta)\rho_{\text{eq}}^\Delta V_0^\dagger(\theta)\sigma_z^j)$. Theoretically, \mathcal{L}_0^Δ is supposed to be a constant due to $V_0^\dagger(\theta) = \mathbb{1}$ for arbitrary θ , while the quantum system in \mathcal{L}_0^Δ and $\mathcal{L}_\delta^\Delta$ both experience the same evolutions, i.e., $U_{\text{E}}(\theta)$ and $U_{\text{E}}^\dagger(\theta)$, which are the main process leading to the decay of signals. In this way, the relative error can be reduced to 0.98% according to the numerical simulation.

- Measurement error:** The measurement error comes from the stochastic fluctuations on NMR signal. Its effect can be calibrated from the signal-to-noise ratio (SNR) of the NMR spectra. To improve the SNR of the ^{31}P channel, protons are decoupled with composite pulses when measuring the signal of ^{31}P nuclear. According to the numerical simulation, the relative error of $\mathcal{L}_\delta^\Delta$ caused by the measurement error decreases from $2.5 \times 10^{-2}\%$ to $1.8 \times 10^{-2}\%$ after applying the decoupling operation.

The analysis above is summarized in Table. S1, which shows that the relaxation contributes to 0.98% relative error and is the main source of errors. This result is close to the experimental error of 1.35%.

QUANTUM STATE TOMOGRAPHY OF 10-SPIN ENGINEERED PROBE

The quantum probe employed in our scheme is the 10-spin star-topology register (STR), which consists of a central spin uniformly interacting with nine peripheral spins. Due to the magnetic equivalence of peripheral spins, they cannot

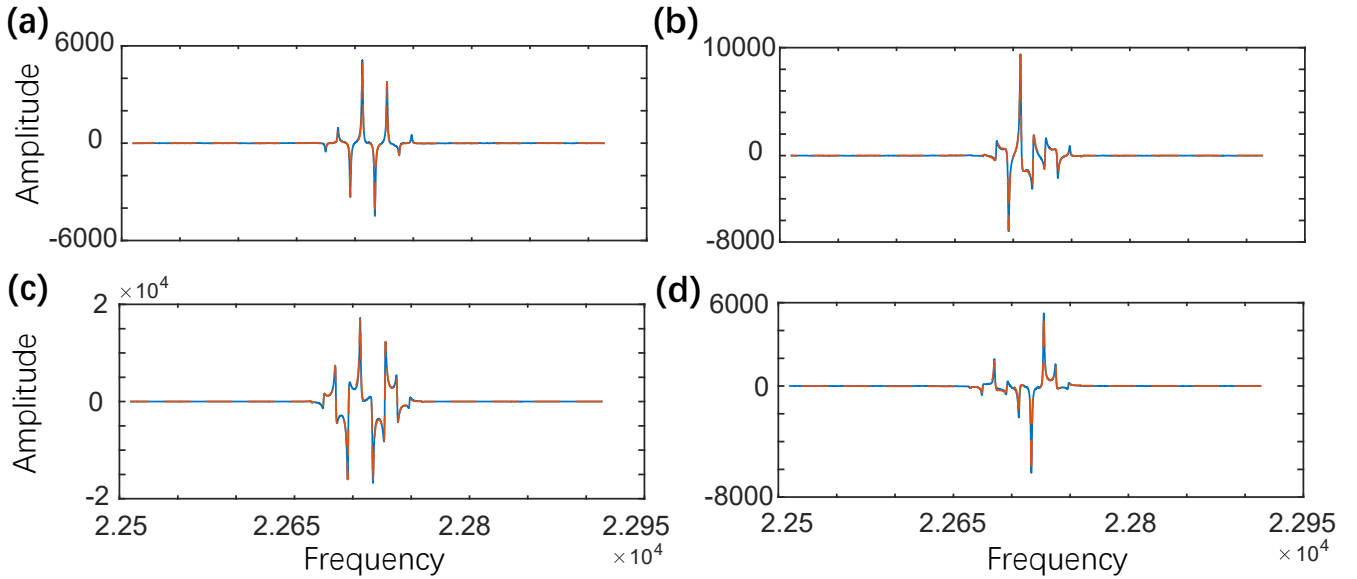


FIG. S4: (a)-(d) are four of the 200 spectra used to construct the density matrix of engineered quantum probe. The blue solid lines are the experimental readouts while the red dashed lines are numerical ones fitted with Lorentz functions. Compared with theoretical results, the relative errors are 9.87%, 8.47%, 5.85% and 11.1%, respectively.

be individually addressed. This also means traditional method of quantum state tomography doesn't apply to this case.

Here we use the method in our recent work Ref. [4]. Specifically, we decompose the Hilbert space of quantum state according to the star-symmetry of STR. In this way, the quantum state can be effectively represented with the minimal degrees of freedom and reconstructed with the minimal readout operations. These readout operations are generated by random PQCs, and the robustness against fluctuation can be further improve by optimizing these PQCs or increase their number.

The minimal number of readout operations that provides complete information of 10-spin STR quantum state is 37. While considering both the consumption of time for experimental measurements and the robustness of reconstruction, we increase the number of measurements to 200. In Fig. S4, we show four of these 200 spectra, where the blue solid lines are the experimental readouts while the red dashed lines are numerical ones fitted with Lorentz functions. Compared with theoretical results, the relative errors in Fig. S4(a-d) are 9.87%, 8.47%, 5.85% and 11.1%, respectively. The theoretical and experimentally reconstructed density matrix are both shown in Fig. S5, where we use the decomposed Hilbert space for simplicity and $\times \cdot$ denotes the number of contained isomorphic subspaces. The accuracy of reconstructed density matrix can be quantified by fidelity. Direct calculation with ρ_f leads to a very high fidelity, as the experimentally measured ρ_f^Δ only takes up a small part of ρ_f . For better quantification of the accuracy, we rewrite the density matrix as

$$\rho_f = \frac{\mathbb{1} + \epsilon \rho_f^\Delta}{2^N} = \frac{1 + \lambda_{\min} \epsilon}{2^N} \mathbb{1} - \lambda_{\min} \epsilon \rho_f'. \quad (\text{S27})$$

Here λ_{\min} is the minimal eigenvalue of ρ_f^Δ , with which ρ_f' is positive semi-definite and $\text{Tr}(\rho_f') = 1$. According to the definition of fidelity between mixed states

$$F(\rho_1, \rho_2) \equiv \left(\text{Tr} \sqrt{\sqrt{\rho_1} \rho_2 \sqrt{\rho_1}} \right)^2, \quad (\text{S28})$$

the fidelity of experimentally reconstructed ρ_f' obtained from 200 readouts is 99.93%. We further calculate its QFI according to Eq. (S8), which is $888\epsilon^2$ with the relative error to theoretical result of 6.62%.

'TIME-REVERSAL-BASED READOUT' PROTOCOL AND ITS PRECISION BOUND

The QFI decides the ultimate potential of quantum state, while this bound can only be saturated under optimal measurements. For an arbitrary nonclassical quantum probe, finding optimal measurements is challenging. Inspired

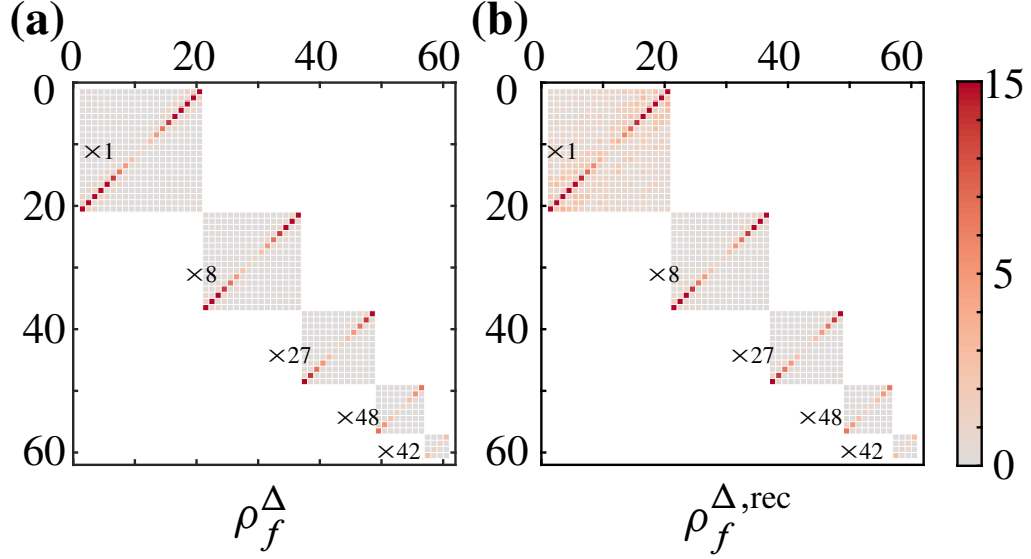


FIG. S5: Deviation density matrix of engineered probe obtained from (a) theoretical calculation and (b) experimentally reconstruction in decomposed Hilbert space, where $\times \cdot$ denotes the number of contained isomorphic subspaces. The fidelity of experimental reconstruction is 99.93%.

by the fact that the 'time-reversal-based readout' can saturate the QCRB for arbitrary pure state [5], we generalize this protocol for mixed probe state. Though this protocol doesn't generate optimal measurements, it virtually saturates the QFI under specific parameters.

The 'time-reversal-based readout' protocol is realized by time reversing the engineering operation U_E and then project onto the initial state. Consequently, it's similar with the protocol for measuring LE except for replacing the quench $e^{-i\delta G}$ with the realistic encoding process $e^{-i\alpha G}$, where α is the unknown parameter. The precision for estimating α is given by standard error propagation

$$(\Delta\alpha)^2 = \frac{(\Delta\mathcal{O})^2}{(d\langle\mathcal{O}\rangle/d\alpha)^2}, \quad (\text{S29})$$

where $(\Delta\mathcal{O})^2 := \langle\mathcal{O}^2\rangle - \langle\mathcal{O}\rangle^2$. For the pure state, the QCRB is saturated when the $\alpha \rightarrow 0$ [1, 5],

$$(\Delta\alpha)^2 = \frac{(\Delta\mathcal{O}_{\text{rev}})^2}{(d\langle\mathcal{O}_{\text{rev}}\rangle/d\alpha)^2}\Big|_{\alpha=0} = \frac{1}{\sqrt{\mathcal{F}(|\Psi_f\rangle)}}. \quad (\text{S30})$$

Here $\mathcal{O}_{\text{rev}} = |\Psi_f\rangle\langle\Psi_f|$ and we use the results

$$\begin{aligned} \Delta\mathcal{O}_{\text{rev}} &= \langle(|\Psi_f\rangle\langle\Psi_f|)^2\rangle - \langle|\Psi_f\rangle\langle\Psi_f|\rangle^2 \\ &= \frac{\alpha^2}{4}\mathcal{F}(|\Psi_f\rangle) + O(\alpha^4) \\ \langle\mathcal{O}_{\text{rev}}\rangle &= 1 - \frac{\alpha^2}{4}\mathcal{F}(|\Psi_f\rangle) + O(\alpha^4), \end{aligned} \quad (\text{S31})$$

where the expectation is taken over the encoded probe, i.e., $\langle\cdot\rangle := \langle\Psi_f|e^{i\alpha G} \cdot e^{-i\alpha G}|\Psi_f\rangle$. For the case of mixed probe,

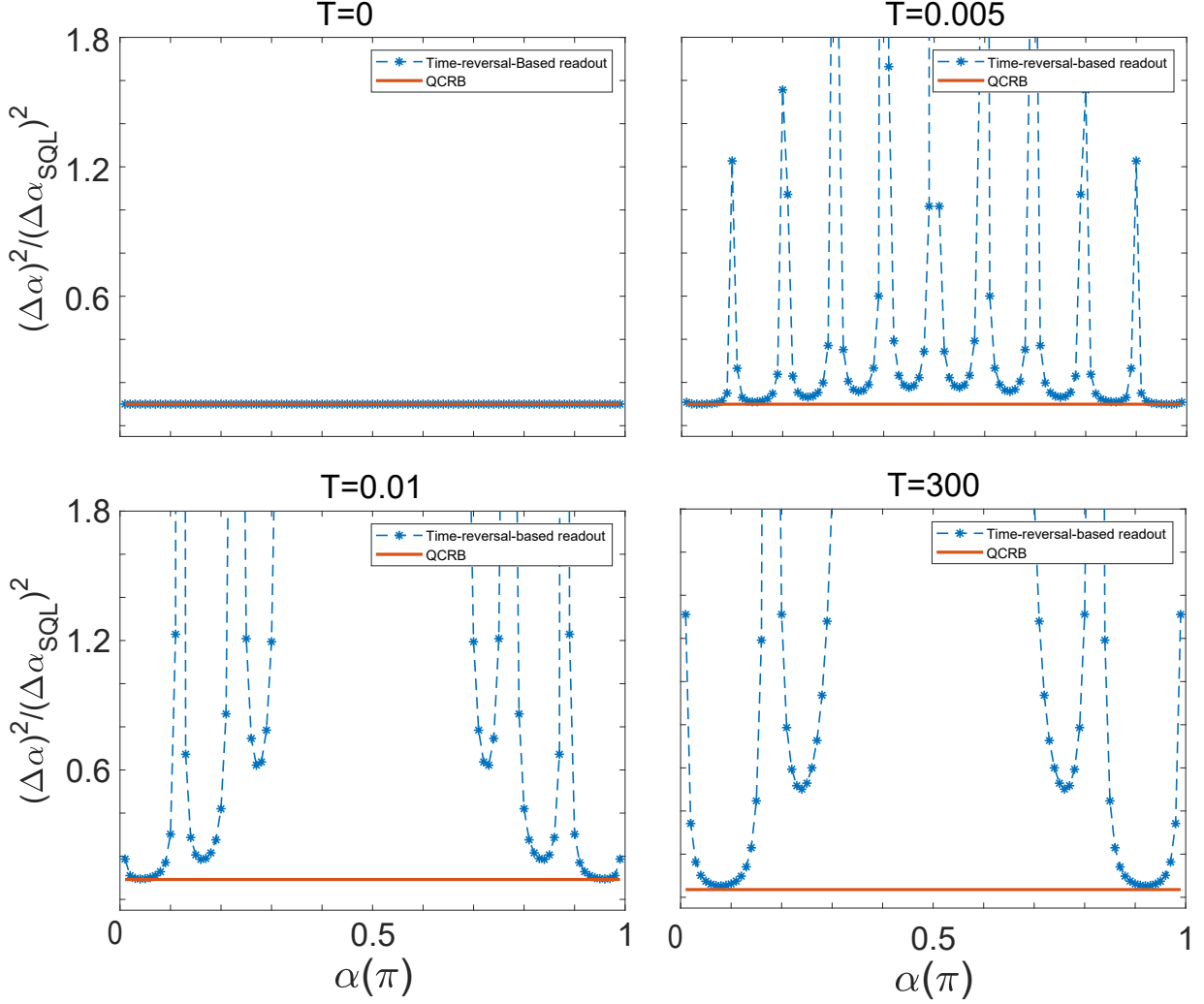


FIG. S6: The ratio of the precision obtained from our 'echo-based protocol' to that of standard quantum limit under different purities. Here the purity depends on the Boltzmann distribution at specific temperature. When the temperature is 0K, the equilibrium state is pure and the precision of 'echo-based protocol' can saturate the QCRB except for the points $\alpha = i\pi/N$ ($i = 1, 2, \dots, N$). The performance of this protocol becomes worse as the increase of temperature, while a precision close to QCRB is still attainable on some specific region of α even at room temperature.

the precision $\Delta\alpha$ can also be obtained from Eq. (S29) by calculating $\langle \mathcal{O}_{\text{rev}} \rangle$ and $\langle \mathcal{O}_{\text{rev}}^2 \rangle$,

$$\begin{aligned}
 \langle \mathcal{O}_{\text{rev}} \rangle &= \text{Tr} \left(e^{-i\alpha G} \rho_f e^{i\alpha G} \rho_f \right) \\
 &= \text{Tr} \left(\sum_{m_1} \rho_{m_1} \sum_{m_2} \rho_{m_2} e^{-im_2\alpha} \right) \\
 &= \sum_m \text{Tr} (\rho_{-m} \rho_m) e^{-im\alpha} \\
 \langle \mathcal{O}_{\text{rev}}^2 \rangle &= \text{Tr} \left(e^{-i\alpha G} \rho_f e^{i\alpha G} \rho_f^2 \right) \\
 &= \sum_{m_1, m_2} \text{Tr} (\rho_{m_1} \rho_{-m_1-m_2} \rho_{m_2} e^{-im_2\alpha}),
 \end{aligned} \tag{S32}$$

where we divide the density matrix of probe into blocks as $\rho_f = \sum_m \sum_{\lambda_i - \lambda_j = m} \rho_{ij} |i\rangle\langle j| = \sum_m \rho_m$ with $G|i\rangle = \lambda_i|i\rangle$ [6]. As $\Delta\alpha$ changes under different α , the protocol can work at the point $\tilde{\alpha} = \text{argmax}_{\alpha} \Delta\alpha$ to obtain the best performance. Though the achievable precision is not optimal, the 'time-reversal-based readout' protocol avoids the cumbersome engineering of optimal measurements and just requires to search the optimum of $\Delta\alpha$. In the following,

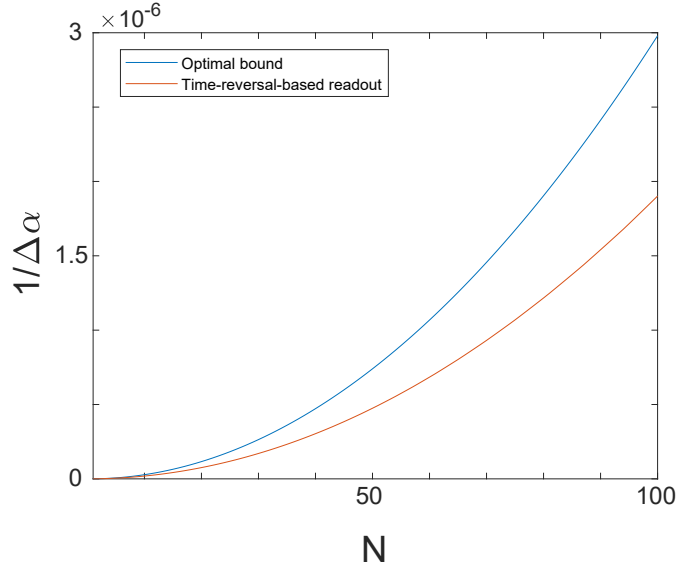


FIG. S7: Scaling of the sensitivity of the 'echo-based readout' protocol (red solid line) in terms of the number of particles when $\epsilon = 10^{-5}$. It can still achieve the Heisenberg scaling with a ratio to the optimal bound given by Ref. [7] (blue solid line) of 0.638.

we give a specific example to show how this protocol works.

To compare the performance of mixed probes with different purity, let us consider the initial probe ρ_0 as the equilibrium state under different temperatures

$$\rho_0 = (\lambda_0|0\rangle\langle 0| + \lambda_1|1\rangle\langle 1|)^{\otimes N}, \quad (\text{S33})$$

where $\lambda_0 = \frac{e^{\hbar\omega/k_B T}}{e^{\hbar\omega/k_B T} + e^{-\hbar\omega/k_B T}}$, $\lambda_1 = \frac{e^{-\hbar\omega/k_B T}}{e^{\hbar\omega/k_B T} + e^{-\hbar\omega/k_B T}}$, $k_B = 1.38 \times 10^{-23} \text{JK}^{-1}$ is the Boltzmann constant, and $|\hbar\omega| = 2.6 \times 10^{-25} \text{J}$ is the energy difference between the Zeeman states for the case of protons in a field of 9.4T [8]. Suppose a near-optimal probe (close to the state given by Eq. (S24)), has been engineered by $U_E(\theta)$, the expression of $\langle \mathcal{O}_{\text{rev}} \rangle$ and $\langle \mathcal{O}_{\text{rev}}^2 \rangle$ can then be obtained from Eq. (S32),

$$\begin{aligned} \langle \mathcal{O}_{\text{rev}} \rangle &= \sum_{i=0}^{\lfloor \frac{N}{2} \rfloor} C_N^i \left\{ \frac{1}{2} (\lambda_0^{N-i} \lambda_1^i + \lambda_0^i \lambda_1^{N-i}) + \frac{1}{2} \cos[(N-2i)\alpha] (\lambda_0^{N-i} \lambda_1^i - \lambda_0^i \lambda_1^{N-i}) \right\} \\ \langle \mathcal{O}_{\text{rev}}^2 \rangle &= \sum_{i=0}^{\lfloor \frac{N}{2} \rfloor} C_N^i \frac{1}{2} \left[(\lambda_0^{N-i} \lambda_1^i)^2 + (\lambda_0^i \lambda_1^{N-i})^2 \right] (\lambda_0^{N-i} \lambda_1^i + \lambda_0^i \lambda_1^{N-i}) \\ &\quad C_N^i \frac{1}{2} \cos[(N-2i)\alpha] \left[(\lambda_0^{N-i} \lambda_1^i)^2 - (\lambda_0^i \lambda_1^{N-i})^2 \right] (\lambda_0^{N-i} \lambda_1^i - \lambda_0^i \lambda_1^{N-i}), \end{aligned} \quad (\text{S34})$$

where C_N^i represents the binomial coefficient. The expression of $\Delta\alpha$ and the corresponding optimal point $\tilde{\alpha}$ can then be obtained. Though the encoded α is unknown, we still can shift it to $\tilde{\alpha}$ with the adaptive method and saturate the local precision limit [9, 10].

In Fig. S6, we show the ratio of the precision obtained from the 'time-reversal-based protocol' to that of standard quantum limit under different temperatures. When the temperature is 0K, the equilibrium state is pure and the precision of 'time-reversal-based protocol' can saturate the QCRB. The performance of this protocol becomes worse as the increase of temperature, while a precision close to QCRB is still attainable on some specific region of α even at room temperature.

We further investigate the scaling of the sensitivity of the 'time-reversal-based readout' protocol. Here, the precision bound is obtained at the optimal point $\tilde{\alpha}$. As shown in Fig. S7, the Heisenberg scaling in terms of the number of particles can still be obtained, whose ratio to the optimal bound in Ref. [7] is 0.638.

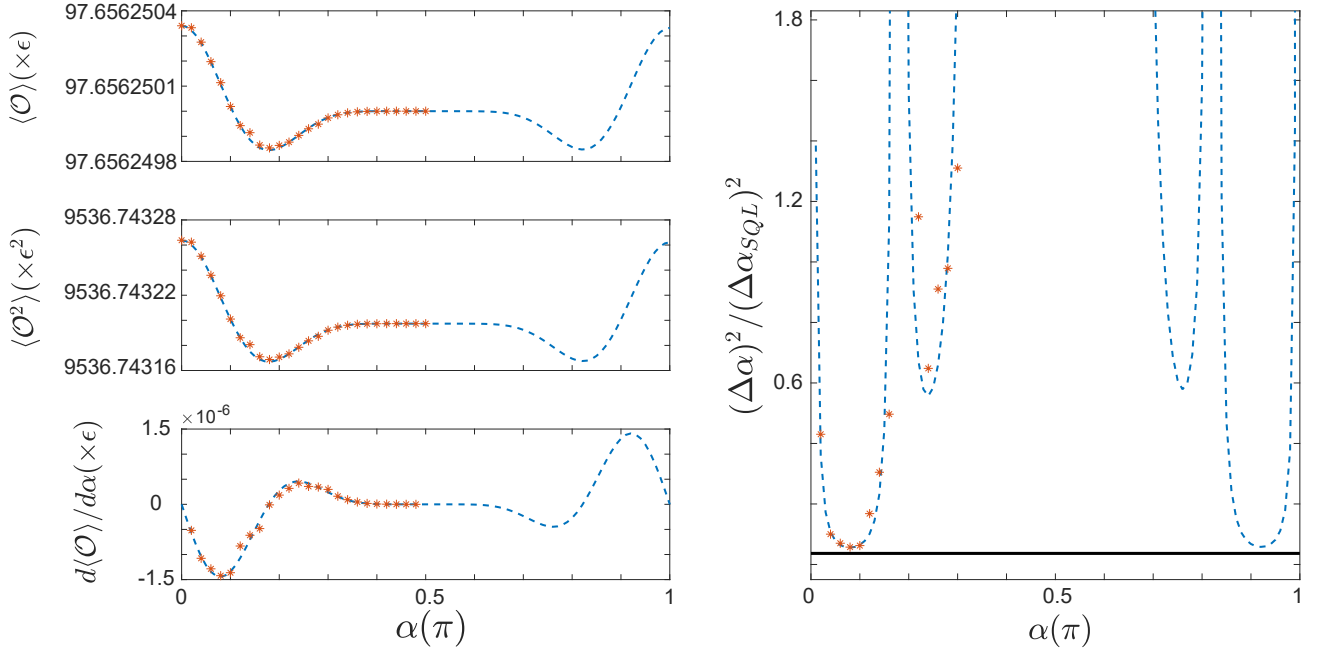


FIG. S8: $\langle \mathcal{O}_{\text{rev}} \rangle$, $\langle \mathcal{O}_{\text{rev}}^2 \rangle$ and $d\langle \mathcal{O}_{\text{rev}} \rangle / d\alpha$ are shown in (a)-(c), where blue dashed lines are theoretical results while red stars are experimental ones. From these results, the precision bound for estimating α , i.e., $\Delta\alpha$ can be calculated. The ratio of $\Delta\alpha$ to standard quantum limit $\Delta\alpha_{\text{SQL}}$ is shown in (d).

EXPERIMENTAL CALIBRATION OF THE PRECISION OF 'TIME-REVERAL-BASED READOUT' PROTOCOL

In the experiment, $\Delta\alpha$ can be calibrated according to Eq. (S29), in which

$$\begin{aligned}
\langle \mathcal{O}_{\text{rev}} \rangle &= \text{Tr} (e^{-i\alpha G} \rho_f e^{i\alpha G} \rho_f) \\
&= \text{Tr} \left(e^{-i\alpha G} U_E \frac{\mathbb{1} + \epsilon \rho_0^\Delta}{2^N} U_E^\dagger e^{i\alpha G} U_E \frac{\mathbb{1} + \epsilon \rho_0^\Delta}{2^N} U_E^\dagger \right) \\
&= \frac{1}{2^N} + \frac{\epsilon^2}{2^{2N}} \text{Tr} (e^{-i\alpha G} \rho_f^\Delta e^{i\alpha G} \rho_f^\Delta), \\
\langle \mathcal{O}_{\text{rev}}^2 \rangle &= \text{Tr} (e^{-i\alpha G} \rho_f e^{i\alpha G} \rho_f^2) \\
&= \text{Tr} \left[e^{-i\alpha G} U_E \frac{\mathbb{1} + \epsilon \rho_0^\Delta}{2^N} U_E^\dagger e^{i\alpha G} U_E \frac{\mathbb{1} + 2\epsilon \rho_0^\Delta + \epsilon^2 (\rho_0^\Delta)^2}{2^{2N}} U_E^\dagger \right] \\
&= \frac{1}{2^{2N}} + \frac{1}{2^{3N}} \text{Tr} [3\epsilon \rho_0^\Delta + \epsilon^2 (\rho_0^\Delta)^2 + 2\epsilon^2 e^{-i\alpha G} \rho_f^\Delta e^{i\alpha G} \rho_f^\Delta] + O(\epsilon^3) \\
&= \frac{1}{2^{2N}} + \frac{\epsilon^2}{2^{2N+2}} \sum_i \gamma_i^2 + \frac{\epsilon^2}{2^{3N-1}} \text{Tr} (e^{-i\alpha G} \rho_f^\Delta e^{i\alpha G} \rho_f^\Delta) + O(\epsilon^3).
\end{aligned} \tag{S35}$$

As $\text{Tr}(e^{-i\alpha G} \rho_f^\Delta e^{i\alpha G} \rho_f^\Delta)$ can be constructed and measured with the same method of $\mathcal{L}_\delta^\Delta$, $\langle \mathcal{O}_{\text{rev}} \rangle$ and $\langle \mathcal{O}_{\text{rev}}^2 \rangle$ can thus be obtained from further calculation. Besides, $d\langle \mathcal{O}_{\text{rev}} \rangle / d\alpha$ is approximated with the difference method

$$\frac{d\langle \mathcal{O}_{\text{rev}} \rangle}{d\alpha} \approx \frac{\langle \mathcal{O}_{\text{rev}} \rangle_{\alpha+\delta'} - \langle \mathcal{O}_{\text{rev}} \rangle_{\alpha-\delta'}}{2\delta'}, \tag{S36}$$

where $\delta\alpha$ is set as $\frac{\pi}{50}$. The experimental results of $\langle \mathcal{O}_{\text{rev}} \rangle$, $\langle \mathcal{O}_{\text{rev}}^2 \rangle$ and $d\langle \mathcal{O}_{\text{rev}} \rangle / d\alpha$ are shown in Fig. S8, and the relative error of directly measured quantity $\text{Tr}(e^{-i\alpha G} \rho_f^\Delta e^{i\alpha G} \rho_f^\Delta)$ is 5.42%.

The precision above corresponds to the precision of a single measurement on ρ_f , which is obtained from the calibrated experimental signals. While in the NMR experiment, there are $\nu \approx 10^{20}$ of independent probes engineered as ρ_f (each being one TMP molecule in the sample). Every measurement of the whole sample amounts to a temporal average of

ν consecutive measurements [11, 12]. According to the central limit theorem, we have the precision for a single NMR measurement

$$\Delta\alpha_{\text{NMR}} = \frac{\Delta\alpha}{\sqrt{\nu}} \approx 1.60 \times 10^{-3}. \quad (\text{S37})$$

* Electronic address: hdyuan@mae.cuhk.edu.hk

† Electronic address: xhpeng@ustc.edu.cn

- [1] T. Macrì, A. Smerzi, and L. Pezzè, *Physical Review A* **94**, 010102 (2016).
- [2] W. Spendley, G. R. Hext, and F. R. Himsforth, *Technometrics* **4**, 441 (1962).
- [3] L. J. Fiderer, J. M. E. Fraisse, and D. Braun, *Phys Rev Lett* **123**, 250502 (2019).
- [4] R. Liu, Y. Hou, Z. Wu, H. Zhou, J. Chen, X. Chen, Z. Li, and X. Peng, arXiv preprint arXiv:2206.08581 (2022).
- [5] S. P. Nolan, S. S. Szigeti, and S. A. Haine, *Phys Rev Lett* **119**, 193601 (2017).
- [6] M. Garttner, P. Hauke, and A. M. Rey, *Phys Rev Lett* **120**, 040402 (2018).
- [7] K. Modi, H. Cable, M. Williamson, and V. Vedral, *Physical Review X* **1**, 021022 (2011).
- [8] M. H. Levitt, *Spin dynamics: basics of nuclear magnetic resonance* (John Wiley and Sons, 2013).
- [9] R. D. GILL, Conciliation of bayes and pointwise quantum state estimation, in *Quantum Stochastics and Information*, pp. 239–261.
- [10] A. Fujiwara, *Journal of Physics A: Mathematical and General* **39**, 12489 (2006).
- [11] M. Schaffry, E. M. Gauger, J. J. L. Morton, J. Fitzsimons, S. C. Benjamin, and B. W. Lovett, *Physical Review A* **82**, 042114 (2010).
- [12] D. Girolami, A. M. Souza, V. Giovannetti, T. Tufarelli, J. G. Filgueiras, R. S. Sarthour, D. O. Soares-Pinto, I. S. Oliveira, and G. Adesso, *Physical Review Letters* **112**, 210401 (2014).